Testing the redox coupling between chromium and nitrogen isotopes in modern and ancient redox-stratified depositional systems: The Coorong Lagoon and the Greater McArthur Basin

Thesis submitted in accordance with the requirements of the University of Adelaide for an Honours Degree in Geology

Savannah Rose Liebelt

November 2019

THE UNIVERSITY of ADELAIDE

TESTING THE REDOX COUPLING BETWEEN CHROMIUM AND NITROGEN ISOTOPES IN MODERN AND ANCIENT REDOX-STRATIFIED DEPOSITIONAL SYSTEMS: THE COORONG LAGOON AND THE GREATER MCARTHUR BASIN

RUNNING TITLE

Testing the redox coupling of Cr and N isotopes

ABSTRACT

The history of Earth's atmospheric oxidation following the Great Oxidation Event (GOE) is widely debated and currently poorly constrained. This uncertainty is largely because the use of different geochemical proxies provides a broad range of possible palaeo-redox conditions during the mid-Proterozoic. Such proxies include nitrogen ($\delta^{15}N$) and chromium ($\delta^{53}Cr$) isotopes, which are the focus of this study. These redox-sensitive proxies have recently demonstrated coupled behaviour in both modern seawaters and recent marine sediments, suggesting isotopic fractionation of Cr could result from biologically-mediated redox cycling of N. This concept is opposed to Cr isotope fractionation being purely representative of oxidative weathering on continents, thus challenging the reliability of the $\delta^{53}Cr$ proxy as a direct tracer for past atmospheric O_2 levels. The aim of this study is to test the purported redox coupling of the $\delta^{53}Cr$ and $\delta^{15}N$ proxies in two redox-stratified depositional systems, specifically investigating (i) modern waters and organic matter from the Coorong lagoon of South Australia, and (ii) organic-rich shales from the greater McArthur Basin in the Northern Territory (including the Velkerri, Mainoru, Barney Creek and Fraynes Formations). These marine settings display notable redox gradients, allowing insight into the isotopic behaviour of N and Cr through a variety of conditions. Contrary to published data, this study revealed no positive co-variance between $\delta^{53}Cr$ and $\delta^{15}N$ records. Rather, $\delta^{15}N$ changes in both waters and shales are interpreted to largely result from pH-driven volatilisation of NH_3, while $\delta^{53}Cr$ variations in shales exhibit a systematic temporal increase. This increase likely reflects progressive basin oxygenation, linked to gradually increasing atmospheric O_2 during the mid-Proterozoic (i.e. from 1.64 to 1.31 Ga). Thus, the validity of $\delta^{53}Cr$ values in marine archives as a palaeo-redox proxy are supported in this instance, with no direct evidence for biologically-driven redox cycling of Cr coupled to local N cycling.

KEYWORDS

Chromium Isotopes, Nitrogen Isotopes, Redox-Stratified Systems, Coorong Lagoon, Greater McArthur Basin, Proterozoic, Palaeo-Redox

TABLE OF CONTENTS

LIST OF FIGURES

LIST OF TABLES

LIST OF EQUATIONS

1. INTRODUCTION

The history of oxygen levels in Earth's atmosphere and its evolution following the Great Oxidation Event (GOE, from around 2.45 to 2.1 Ga) is widely debated and currently poorly constrained (Large et al., 2019; Lyons, Reinhard, & Planavsky, 2014). In particular, atmospheric oxygen levels during the mid-Proterozoic (between 1.8 and 0.8 Gyr) are inadequately established, largely because different geochemical proxies provide a broad range of possible palaeo-redox conditions (from <0.1 to 10% of present atmospheric O_2 levels, PAL) (Ozaki, Reinhard, & Tajika, 2019). Stable chromium isotopes ($\delta^{53/52}Cr$), the primary focus of this thesis, have recently been studied in marine archives to further constrain palaeo-redox conditions during the mid-Proterozoic. However, results have been conflicting, with Cr isotopes alone suggesting a difference in atmospheric O_2 from below 0.1% PAL (Planavsky et al., 2014) to above 1% PAL (Canfield et al., 2018; Large et al., 2019) (see Figure 1). Other studies, based on different palaeo-redox proxies, also imply a range of atmospheric O_2 levels, with some suggesting a stepwise development during the Proterozoic (Figure 1a). A relatively short-lived atmospheric oxygen "overshoot" following the GOE is proposed, rising to near-modern levels (close to 20 wt.% O_2), before a marked drop during the mid-Proterozoic and an eventual recovery to modern-like levels following the Neoproterozoic Oxygenation Event (NOE) (Fakhraee, Hancisse, Canfield, Crowe, & Katsev, 2019; Lyons et al., 2014).

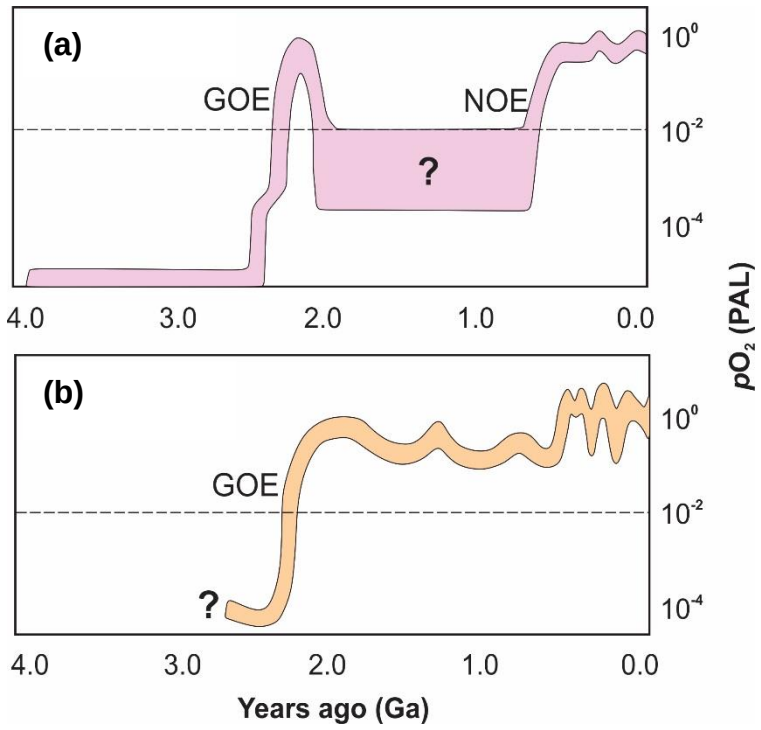

Figure 1: Contrasting models of atmospheric oxygenation, using a variety of proxies but not including Cr. (a) The top curve shows the evolution of pO_2 (atmospheric partial pressure of O_2) proposed by Lyons et al. 2014, including an overshoot at the GOE and an uncertain central period where levels appear to have dropped to below 0.1% of present atmospheric levels (PAL). This model also includes a second surge at the NOE between 0.635 and 0.55 Ma. (b) The second curve, proposed by Large et al. 2019, suggests a cyclic oxygenation with a mean pO_2 of approximately 10^{-1} times PAL, consistently higher than previously accepted.

Rather than looking at Earth's atmospheric oxygenation as a series of distinct events separated by periods of relative stability, it could also be perceived as a continuous process towards progressively more oxic conditions (Figure 1b), superimposed on short-term oscillations in atmospheric O_2 levels through the Proterozoic and Phanerozoic (Large et al., 2019).

Importantly, the onset of free oxygen production has been linked not only to the Earth's atmospheric oxygenation, but also to major evolutionary steps (Reinhard, Planavsky, Olson, Lyons, & Erwin, 2016). However, the current uncertainty about the plausible range of atmospheric O_2 levels during the mid-Proterozoic sustains the debate about the timing and causative links with the emergence of complex multi-cellular life

(Gilleaudeau et al., 2016). Other poorly constrained links include the control of plate-tectonic induced mountain building and volcanism (i.e. emissions of reduced volcanic gases) on atmospheric O_2 levels (Campbell & Allen, 2008; Large et al., 2019), as well as the positive feedback between nutrient supply, bio-productivity and O_2 availability (Reinhard, Planavsky, Ozaki, et al., 2016; Tribovillard, Algeo, Lyons, & Riboulleau, 2006). With such major implications for tectonic and biological evolution of our planet, it is therefore of primary importance to earth system studies and palaeo-biology to more tightly constrain the redox history of the ocean-atmosphere system.

Recently, the isotopic composition of redox sensitive elements have been used to determine paleo-redox conditions of the ancient ocean-atmosphere system, allowing further testing of scenarios proposed for atmospheric oxygenation. In particular, the application of nitrogen (N) isotopes (Casciotti, 2016), and chromium (Cr) isotopes (Gilleaudeau et al., 2016) has become established for palaeo-redox reconstructions, along with a new multi-proxy approach combining both $\delta^{15}N$ and $\delta^{53}Cr$ tracers (Gueguen et al., 2016; Moos, 2018). Pioneering studies on chromium isotopes in modern and ancient marine environments have confirmed its redox sensitivity (Farkaš et al., 2018; Frei, Gaucher, Poulton, & Canfield, 2009). However, there is still uncertainty regarding the threshold at which Cr isotopes will respond to redox changes, causing the validity of this proxy to be called into question (Large et al., 2019). This prompts the suggestion that Cr isotope fractionation in marine environments could be linked with nitrogen and/or manganese (Mn) cycling, including microbial redox processes such as nitrification and denitrification associated with Cr reduction (see Figure 2 and Gueguen et al., 2016; Moos, 2018), and/or Mn-oxidation facilitating in-situ Cr oxidation (Miletto et al., 2019). These new findings raise doubt on the traditional interpretation that marine

δ^{53}Cr values solely record changes in oxidative weathering, linked directly to atmospheric oxygen concentrations (Frei et al., 2009; Planavsky et al., 2014; Remmelzwaal et al., 2019), or if perhaps Cr isotope variations instead reflect local redox processes controlled by biological activity.

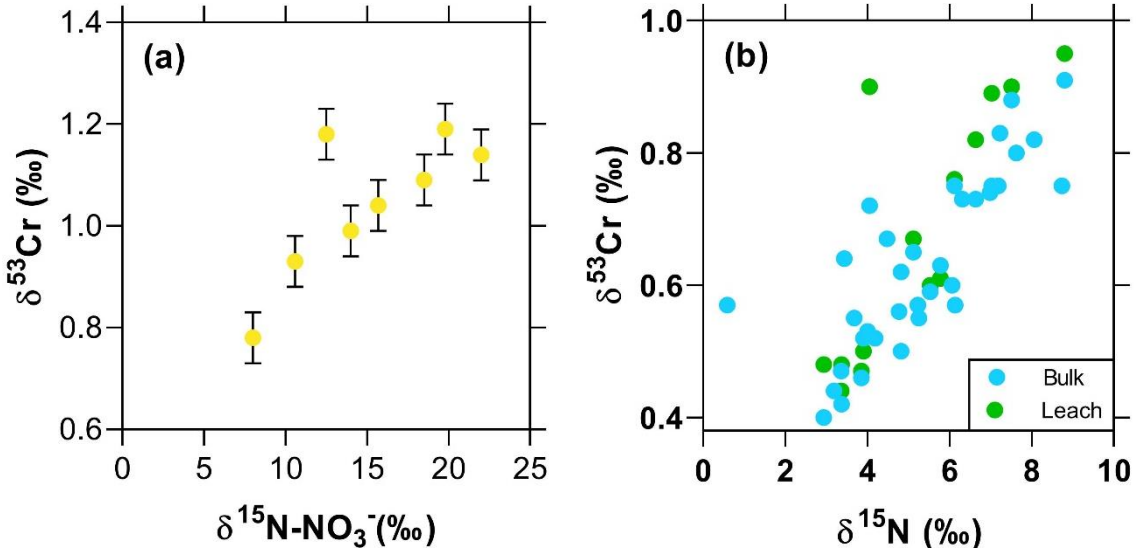

Figure 2: Cross-plots of chromium isotopes (δ^{53}Cr relative to NIST SRM 979) and nitrogen isotopes (δ^{15}N relative to AIR) from different studies. (a) δ^{53}Cr and δ^{15}N of nitrate in modern ocean waters sampled from the Santa Barbara Basin near Mexico. These oxygen deficient waters experience periodic renewal of bottom waters and high primary productivity near the surface. A strong correlation is observed between these two redox isotope tracers (R^2 = 0.91, n = 7, thus not considering the one outlier), suggesting direct control of microbial reduction on Cr isotopes and Cr(VI) cycling in the oxygen minimum zone (Moos, 2018). (b) δ^{15}N and δ^{53}Cr of bulk and leached marine sediments from the Peru Margin, also showing a strong positive correlation (R^2 = 0.88, n = 47, thus not considering the two outliers). This relationship is explained by possible expansion of the oxygen minimum zone during interglacial periods, with the resulting changes in biological activity also influencing the Cr isotope signature which is stored in the sedimentary archive (Gueguen et al., 2016).

This study will test such purported links between the marine cycling of N and Cr, driven by local microbial redox processes, to further assess the applicability of the chromium isotope proxy for past atmospheric O_2 reconstructions. This will be achieved by investigating the relationships between chromium and nitrogen isotopes in modern and ancient marine environments with large redox gradients (from oxic to sub-oxic, anoxic). The Coorong lagoon system in South Australia will be utilised as a modern analogue for

a redox-variable marine system (Shao et al., 2018), where $\delta^{53}Cr$ and $\delta^{15}N$ in local waters are aimed to be calibrated against variable dissolved O_2 concentrations, to assess the proposed links with oxygen levels (Frei et al., 2009; Planavsky et al., 2014). Additionally, marine sedimentary archives (i.e. organic-rich shales) from the greater McArthur Basin in the Northern Territory will be used to explore palaeo-redox conditions and internal cycling of N and Cr in an ancient redox-stratified system, to test if these proxies do indeed record the mid-Proterozoic evolution of oxygen in the ocean-atmosphere system (Cox, Sansjofre, Blades, Farkas, & Collins, 2019), or rather some local biologically-controlled redox processes. The latter would be expected to manifest as coupled $\delta^{53}Cr$ and $\delta^{15}N$ records, such as those documented by Moos (2018) and Gueguen et al. (2016) in both modern seawaters and recent marine sediments (Figure 2).

2. BACKGROUND

As this study is exploring the possible connection between the redox cycling of nitrogen and chromium isotopes, an overview of their biogeochemistry and isotopic systems is presented below.

2.1 Nitrogen as a redox proxy

Nitrogen (N) is an essential element for life, imparting a major control on modern biological productivity. With speciation and isotopic composition controlled by redox conditions, nitrogen has been found to be closely linked with atmospheric and oceanic oxidation states throughout geological history (Glibert, Middelburg, McClelland, & Vander Zanden, 2019), despite the significant complexity of the biogeochemical nitrogen cycle (Casciotti, 2016).

Nitrogen is present in many forms, with transformations occurring via a number of processes (Figure 3). Some pathways followed in the ocean include nitrification, denitrification, and biological fixation. Nitrification involves the bacterial and archaeal (prokaryotic) oxidation of bioavailable ammonium (NH_4^+) to nitrate (NO_3^-) under oxic to sub-oxic conditions (Korth, Kock, Arévalo-Martínez, & Bange, 2019). The onset of widespread nitrification has been connected with the appearance of oxygenic photosynthesis and accumulation of O_2 in the aftermath of the GOE, with correlated presences of NO_3^- and O_2 interpreted from other proxies (Stüeken et al., 2016; Thomazo & Papineau, 2013). Comparatively, denitrification involves the reduction of nitrate under anoxic to sub-oxic conditions, also with bacterial influence (Casciotti, 2016).

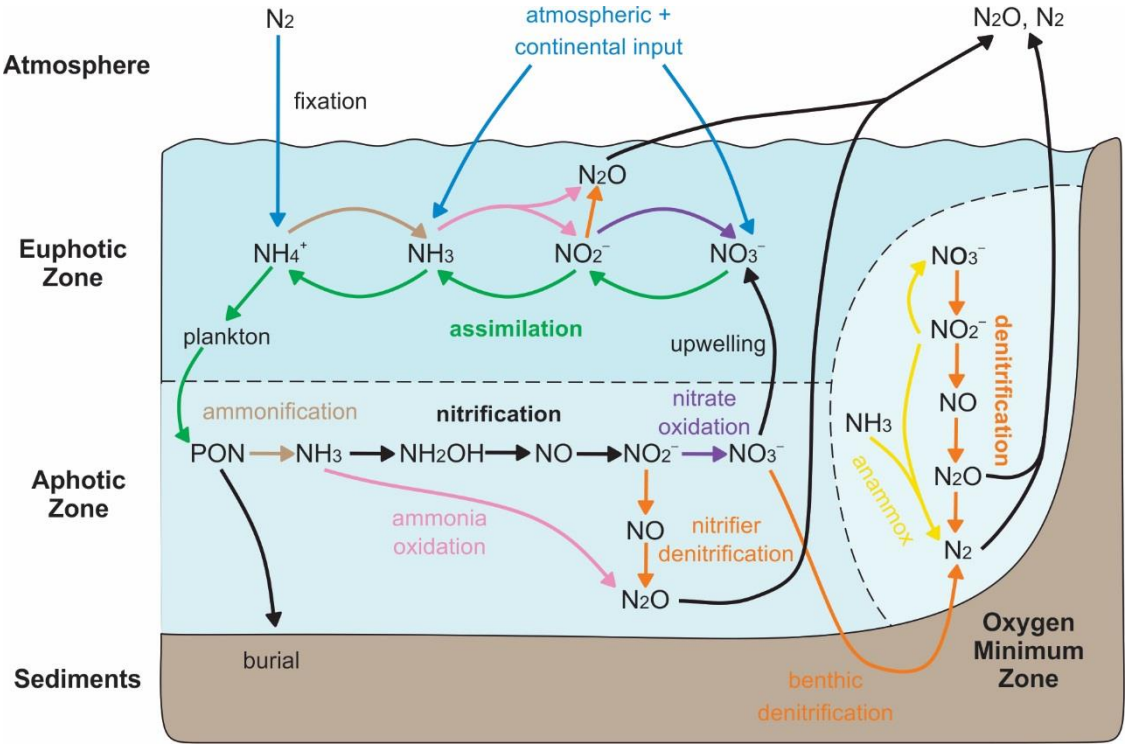

Figure 3: Overview of the complex marine N cycle. Processes shown are controlled by varying states of oxygenation and primary productivity. Inputs (N_2 fixation and atmospheric and continental inputs) are shown in blue, and losses are shown in orange (denitrification) or yellow (anammox). Internal processes are coloured green (PON production through assimilation or planktonic grazing), brown (remineralisation through ammonification), pink (remineralisation through nitrification and ammonia oxidation) and purple (remineralisation through nitrite oxidation). Physical processes (upwelling, export of sinking PON, burial, and gaseous exchange between the air and ocean) are shown in black. Adapted from Sigman et al. (2009), Casciotti (2016), and Korth et al. (2019).

During some of these biotic and abiotic processes, isotopic fractionation occurs (Table 1). This fractionation is expressed in delta notation as $\delta^{15}N$, with $^{15}N/^{14}N$ ratios normalised to atmospheric nitrogen (AIR). Nitrification typically leaves the resultant NO_3^- isotopically lighter (i.e. with negative or lower $\delta^{15}N$ signatures) than the original biomass. Comparatively, denitrification returns isotopically light N_2 to the atmosphere, leaving the residual nitrate pool enriched in heavier ^{15}N (i.e. with positive or higher $\delta^{15}N$ signatures) (Sigman et al., 2009). Biological fixation (diazotrophy) occurs when cyanobacteria directly fix inorganic atmospheric N_2 into bioavailable ammonium and/or ammonia (NH_3), or particulate organic nitrogen (PON). This process typically goes to completion, resulting in minimal isotopic fractionation (Michener & Lajtha, 2007).

Table 1: Biotic and abiotic nitrogen pathways and their associated isotopic fractionations. Some processes such as nitrification, denitrification and anammox include a number of intermediate steps, but only the key reactant and product are indicated here. Fractionations are defined as $\varepsilon \approx \delta^{15}N_{product} - \delta^{15}N_{reactant}$

Process	Species Converted	Fractionation (‰)	Source
Fixation	N_2 → NH_4^+ (PON)	-3 to +1	Casciotti (2016)
Ammonification	NH_3 → NO_2^-	+1	Stüeken et al. (2016)
Nitrification	NH_3 → NO_3^-	-1 to -25	Stüeken et al. (2016)
Ammonia oxidation	NH_3 → NO_2^-	+12 to +38	Sigman et al. (2009)
Nitrite oxidation	NO_2^- → NO_3^-	-20 to -7	Casciotti (2016)
Water column denitrification	NO_3^- → N_2	+25 to +39	Sigman et al. (2009), Michener and Lajtha (2007)
Benthic/sedimentary denitrification	NO_3^- → N_2	0 to +4	Casciotti (2016)
Anammox	NO_2^- + NH_4+ →N_2	-31	Casciotti (2016)
DNRA (dissimilatory nitrate reduction to ammonia)	NO_3^- → NH_4^+	+20 to +30	Casciotti (2016)
Anammox (anaerobic ammonium oxidation)	NH_3 → N_2	-26 to -16	Stüeken et al. (2016)
Assimilation	NH_4^+ → PON	+15	Sigman et al. (2009)
Volatilisation	NH_4^+ → NH_3 → N_2	-45 to -29	Stüeken et al. (2016), Michener and Lajtha (2007)
Remineralisation	PON → NO_3^-	+3	Sigman et al. (2009)

Importantly, N isotopes in oxygen poor (i.e. anoxic, sub-oxic) and nutrient-rich restricted marine settings, dominated by reduced NH_4^+ and NH_3 species, can also be

fractionated inorganically via evaporation and volatilisation of NH_3, associated with large N isotope fractionations (up to 45‰, see Table 1). This volatilisation can generate large positive $\delta^{15}N$ anomalies in the remaining NH_4^+ pool and/or organic matter (PON) that forms from this isotopically heavy ammonium reservoir (De Brabandere et al., 2007). Ultimately, it is these varying degrees of fractionation, occurring as a function of fluctuating redox states and primary productivity, which can be used as a proxy to constrain atmospheric oxygen levels through geological history (Cox et al., 2019; Stüeken et al., 2016).

2.2 Chromium as a redox proxy

Chromium is a redox-sensitive transition metal with two main oxidation states, reduced Cr(III) and oxidised Cr(VI). Both are present in near-surface environments, typically controlled by the availability of free O_2 and Mn-oxides (oxidants) compared to reduced Fe(II) species or organic matter (reductants). Thus, oxidative weathering on continents in an O_2 rich atmosphere, and/or reduction in the ocean via Fe(II) and organic matter, can control the redox cycling and abundance of Cr(VI) and Cr(III) species, and therefore also Cr isotope fractionation.

Similarly to nitrogen, chromium isotope fractionation is expressed as $\delta^{53}Cr$, with $^{53}Cr/^{52}Cr$ ratios normalised against the standard of NIST SRM 979 (chromium nitrate) (Paulukat, Gilleaudeau, Chernyavskiy, & Frei, 2016). During oxidative weathering, reduced and particle-reactive Cr(III) can be oxidised to mobile Cr(VI), catalysed by manganese oxides (Figure 4). This mobile and oxidised Cr(VI) can subsequently enter the ocean via riverine transport, accompanied by a partial back-reduction to Cr(III) via interaction with Fe(II) or organic matter. This back-reduction is associated with Cr

isotope fractionation, leaving the remaining soluble and dissolved Cr(VI) in rivers, streams and eventually oceans enriched in heavy Cr isotopes (i.e. with positive or higher δ^{53}Cr signatures). Lighter ^{52}Cr becomes enriched in immobile Cr(III) species produced during the above partial reduction. Once in the ocean and under anoxic conditions, this positively fractionated Cr(VI) can then experience complete or quantitative reduction back to Cr(III) during so-called "reductive deposition", before eventual incorporation into marine sediments. A complete list of processes causing isotopic fractionation of Cr during continental weathering and marine deposition is detailed in Table 2 and illustrated in Figure 4.

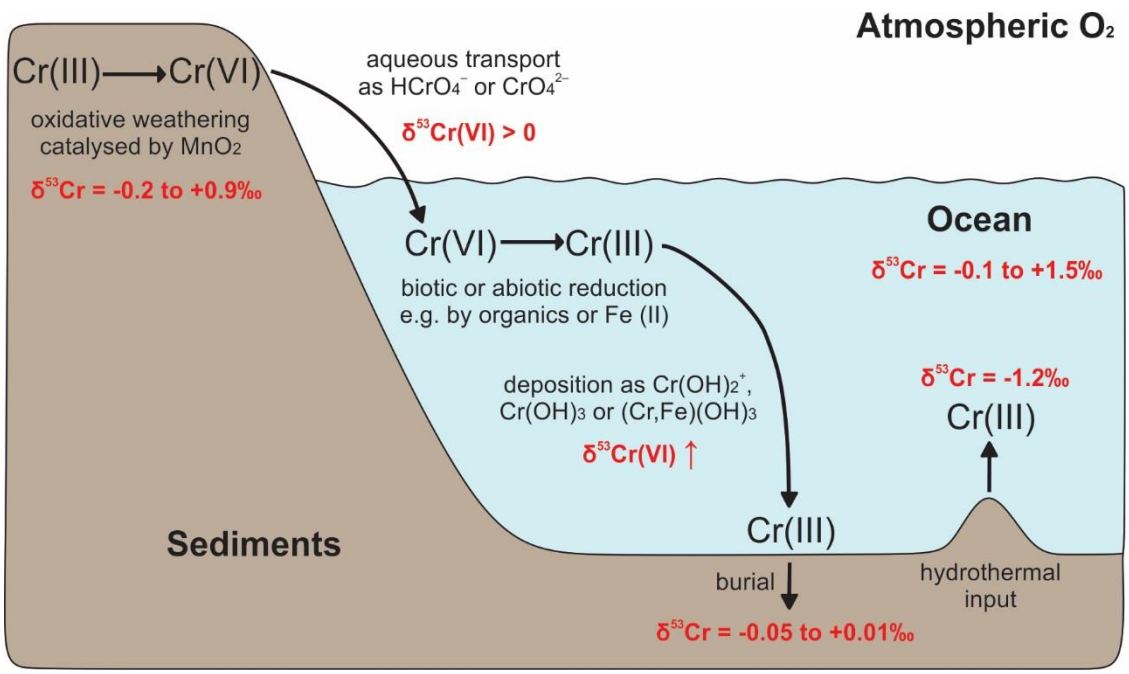

Figure 4: Schematic of the modern biogeochemical chromium cycle. Oxidative weathering of Cr(III) to Cr(VI) in soils is catalysed by MnO_2, allowing Cr(VI) to be transported to the ocean via riverine transport as mobile CrO_4^{2-} or $HCrO_4^-$ species. This transport is accompanied by partial back-reduction by Fe(II) or organic matter, causing an enrichment of the heavier ^{53}Cr in the remaining Cr(VI) pool being transported. Once in the ocean, Cr can be further reduced by reductants including Fe(II) acid volatile sulphides, organic matter and organic ligands. The resultant Cr(III) forms cations such as $Cr(OH)_2^+$, $Cr(OH)_3$ and $(Cr,Fe)(OH)_3$, which readily form complexes with Fe- and Mn-oxyhydroxides and are removed via burial into the authigenic fraction of marine sediments. The Cr isotopic value stored in marine sediments will therefore reflect the occurrence and intensity of oxidative weathering of Cr on continents. Adapted from Frei (2009), Bruggmann (2018) and Birte Frank (2019).

Table 2: Range of chromium isotope fractionations associated with a variety of redox reactions under low temperature surface conditions. Fractionations are defined as $\varepsilon \approx \delta^{53}Cr_{product} - \delta^{53}Cr_{reactant}$. Table has been adapted from Bruggman (2018).

Process	Reactant	Fractionation (‰)	Source
Reduction	Fe compounds	-4.3 ± 0.11 to -1.50	Kitchen et al. (2012), Døssing et al. (2011) Sikora, Johnson, and Bullen (2008), Han, Qin, Brown, Christensen, and Beller (2012)
	Bacteria	-4.1 to -0.4 ± 0.2	Jamieson-Hanes, Amos, and Blowes (2012) Zink, Schoenberg, and Staubwasser (2010)
	Organic C	-3.51 to -2.10	
	H_2O_2	-5.00 to -3.54	
Oxidation	Birnessite (Mn oxide)	-2.5 to +0.7	Bain and Bullen (2005), Miletto et al. (2019)
	H_2O_2	+0.2	Zink et al. (2010), Oze, Bird, and Fendorf (2007), Izbicki, Ball, Bullen, and Sutley (2008)
	weathering of Cr(III) bearing rocks		
Complexation	Organic acids, siderophores	-0.27 to +1.23	Saad et al. (2017)
Sorption	Al-oxides, geothite	< -0.04	Ellis, Johnson, and Bullen (2004)
Isotope exchange	Cr(III) to Cr(VI), 25°C	+6 to +7	Schauble, Rossman, and Taylor (2004)
Incorporation	Corals	-0.92 ± 0.2	Pereira et al. (2016)
	Bivalves	-0.4 to -0.3	Frei, Paulukat, Bruggmann, and Klaebe (2018)
	Marine biogenic carbonates	-0.7 to 0.0	Farkaš et al. (2018)
	Inorganic carbonate	+0.06 to +0.29	Rodler, Sanchez-Pastor, Fernandez-Diaz, and Frei (2015)

Therefore, the isotopic composition of Cr in marine archives should provide a first-order proxy for the presence of Cr(VI) in ancient surface waters following oxidative weathering, thus providing information on the oxidative state of Earth's atmosphere in geological history (Gueguen et al., 2016; Tribovillard et al., 2006). With estimates of chromium's oceanic residence time ranging from 3000 years (Moos, 2018) to 9000 years (Frei et al., 2009), it is supposed that chromium could be a valuable tracer of geologically short-term oxygen perturbations in the global oceans.

2.3 The Coorong lagoon system

The modern Coorong lagoon of South Australia (Figure 5) represents a unique hydrologically connected lagoonal system, creating an analogue for palaeo-redox studies in semi-restricted systems such as the greater McArthur Basin (Bullen, 2017). It forms settings ideal for exploring the behaviour of traditional and novel isotopes such as nitrogen and chromium, with a range of redox conditions (from 2.53 to 15.6 mg/L O_2) and other environmental parameters including salinities (Shao et al., 2018).

The 110 km long Coorong lagoon, split into the North and South Lagoons, experiences partial restriction from the ocean while accommodating mixing of continental-sourced freshwater and seawater from the Southern Ocean. The North Lagoon receives water mostly from the ocean and Lower Lakes, with the latter fed via the Murray Mouth occasionally from the release of freshwater through barrages (Mosley, Hamilton, Busch, Hipsey, & Taylor, 2017; Phillips & Muller, 2006). Comparatively, the South Lagoon is more hydrologically restricted (Reid & Mosley, 2016), being separated from the ocean by Holocene-aged sand dunes (Kjerfve, 1986; Knoppers, 1994) and with limited connection to the North Lagoon due to the naturally occurring Parnka Point barrier (Figure 5). As a result, local waters can range from virtually fresh if dominated by inputs from the River Murray and Lower Lakes, to mostly marine in the North Lagoon, with up to hypersaline conditions typical for the South Lagoon (Haese, Murray, & Wallace, 2009). Oxygen levels in lagoon waters also range from fully oxic in the North Lagoon to sub-oxic/anoxic mostly in the South Lagoon, and especially near the Parnka Point barrier (Webster, 2010).

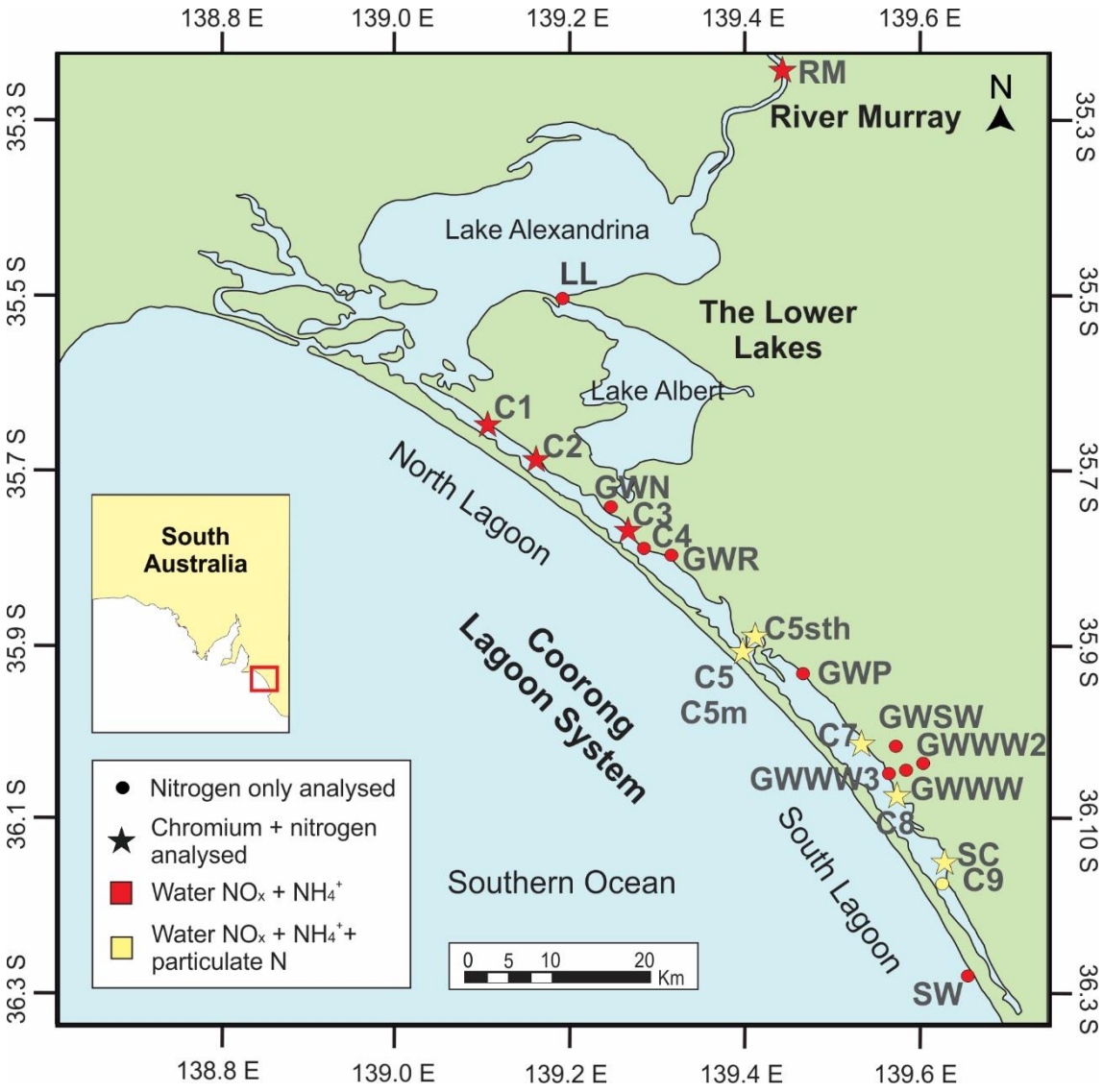

Figure 5: Map of the Lower Lakes and Coorong region in South Australia (adapted from Webster 2010), indicating approximate sampling locations for this study and analyses conducted on samples from each site. Samples C5, C5m and C5sth are all located at Parnka Point, the natural barrier located in the middle of the system which separates the North and South Lagoons. Precise coordinates for sampling sites can be found in Appendix A.

2.4 McArthur Basin

With the Coorong lagoon providing a modern analogue, the greater McArthur Basin (Figure 6), located in the northeast of the Northern Territory, Australia, is explored as an ancient redox-stratified basin. This depositional system allows insight into isotopic behaviour during the mid-Proterozoic, when atmospheric oxygen levels are only beginning to be unravelled.

The McArthur Basin is a large intra-cratonic depositional system covering an area of approximately 180,000 km^2, containing successions of Palaeoproterozoic to Mesoproterozoic aged sedimentary rocks. These sedimentary sequences include the Tawallah, McArthur, Nathan and Roper Groups (Ahmad, Dunster, & Munson, 2013). In this study, geochemical and isotope analyses were focused on organic-rich shales of different ages from three formations in the McArthur Basin. Specifically, these were the Velkerri, Mainoru and Barney Creek Formations (Figure 7).

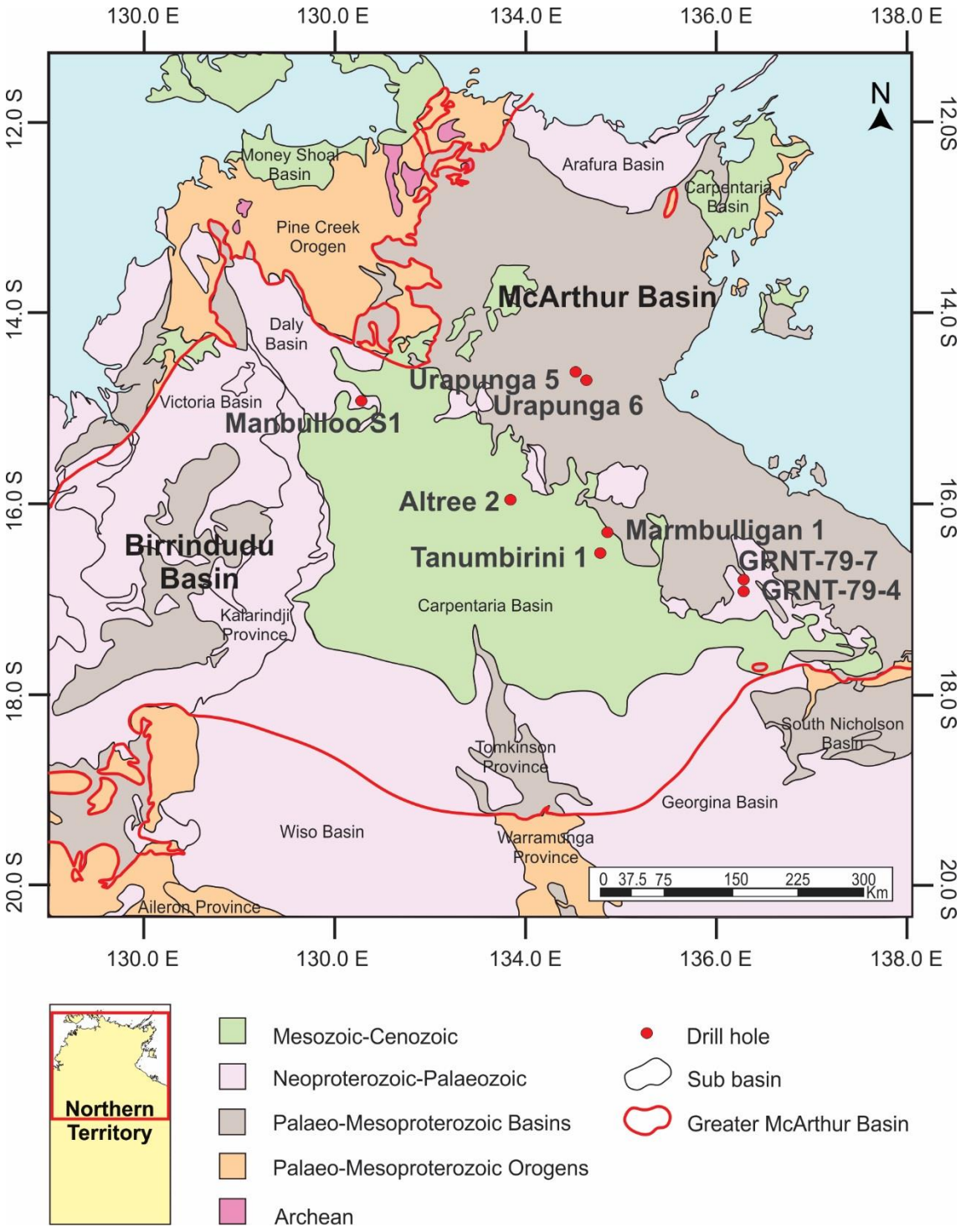

Figure 6: Geological map of the Northern Territory, showing all major basins and sub-basins, as well as the locations of drill holes containing samples for this study. Specifically, the samples from the Velkerri Formation come from Altree 2, Marmbulligan 1 and Tanumbirini 1 drill holes. The Mainoru Formation is explored using the Urapunga 5 and Urapunga 6 drill holes, and the Fraynes Formation was collected from the Manbulloo S1 drill hole. The Barney Creek Formation has been sampled using the GRNT-79-4 and GRNT-79-7 drill holes. This map has been adapted from the Northern Territory Geological Survey (NTGS) Strike database, with all coordinates outlined in Appendix A.

The Velkerri Formation was deposited between 1.349 and 1.312 Ga (Yang et al., 2018), and is an organic-rich mudstone/siltstone interpreted to have been deposited in a deltaic to distal shelf environment (Sheridan, Johns, & Johnson, 2018) during the post-rift phase of basin development. It is well preserved and largely undeformed, making it a favourable sedimentary archive for isotope studies of Mesoproterozoic palaeo-environmental conditions in the McArthur Basin (Rafiei & Kennedy, 2019). The Mainoru Formation is approximately 1.492 ± 0.004 Ga (Jackson, Sweet, Page, & Bradshaw, 1999), with its two youngest members being investigated here. The Showell Member is a laminated calcareous mudstone understood to have been deposited in a distal to storm-dominated shelf. The slightly older Wooden Duck Member is a grey-green mudstone to micaceous sandstone inferred to have been deposited in a storm-dominated shelf (Yang et al., in press). Finally, the Barney Creek Formation, deposited in an actively subsiding section of the southern McArthur Basin around 1.640 ± 0.004 Ga (Ahmad et al., 2013; Page, Jackson, & Krassay, 2000), mostly consists of carbonate, dolomite and organic-rich siltstone and shale (Schmid, 2015).

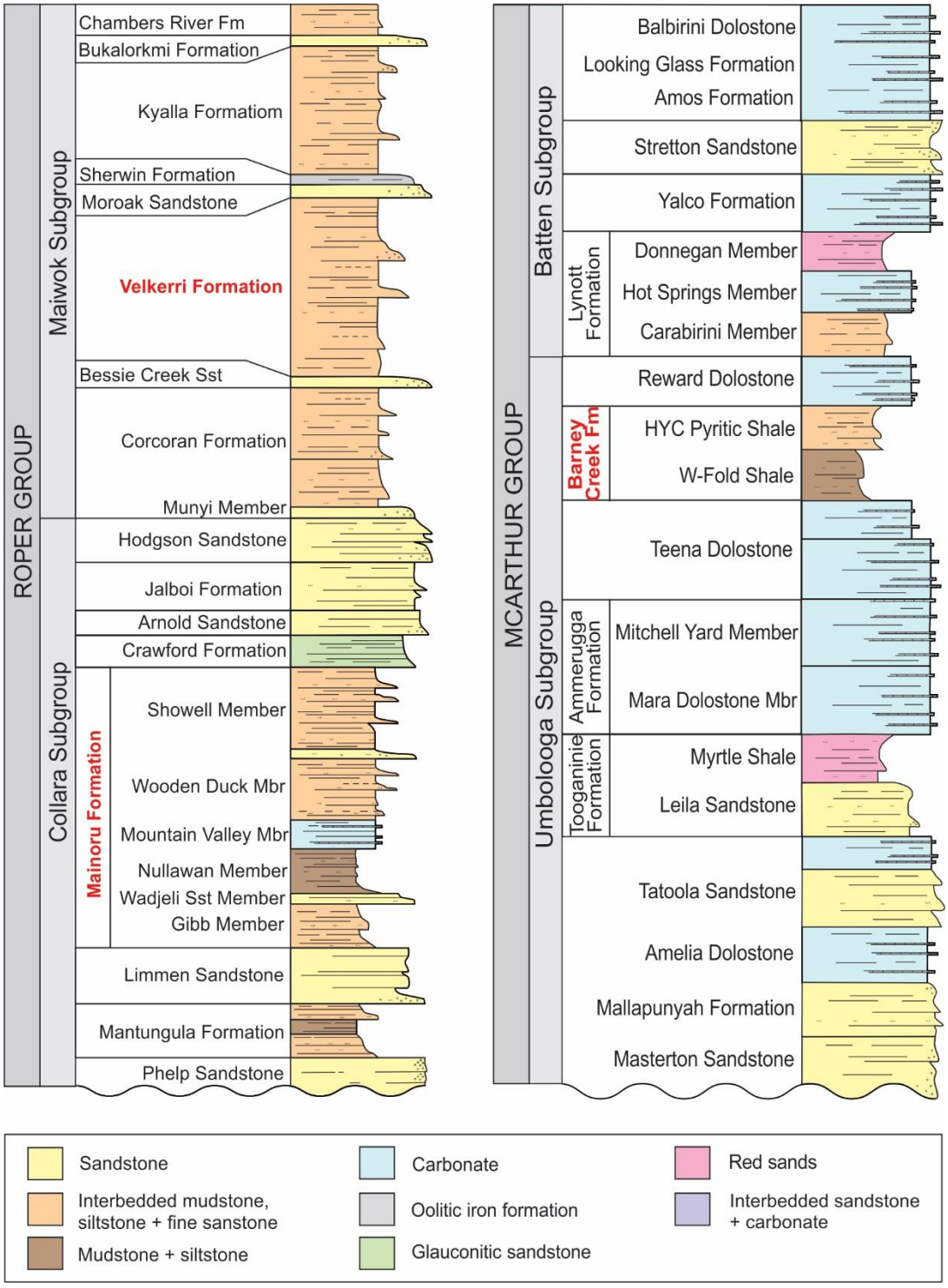

Figure 7: Stratigraphic columns of the Roper Group (left) and McArthur Group (right) from the McArthur Basin. The Roper Group contains the Velkerri and Mainoru Formations, which are investigated here and dominated by siliciclastic systems, while the McArthur Group contains the older Barney Creek Formation, from a carbonate dominated depositional system. Note that thickness illustrated here are representative only. Adapted from Ahmad et al. (2013).

2.5 Birrindudu Basin

The Birrindudu Basin is considered a sub-basin within the greater McArthur Basin (Figure 6) and correlates with the McArthur Basin (Rawlings, 1999), also being Palaeoproterozoic to Mesoproterozoic in age. It crops out over 35,000 km^2 in the Northern Territory alone, and extends further under cover into Western Australia. In this basin, the Fraynes Formation of the Limbunya Group is explored (Figure 8). This micaceous siltstone with organic-rich units has an increasing presence of carbonate up-section, and was deposited in a nearshore shallow marine environment around 1.638 ± 0.009 Ga (Ahmad & Munson, 2013). As such, it is interpreted as a time equivalent to the Barney Creek Formation deposited in the more central part of the greater McArthur Basin (Munson, 2019).

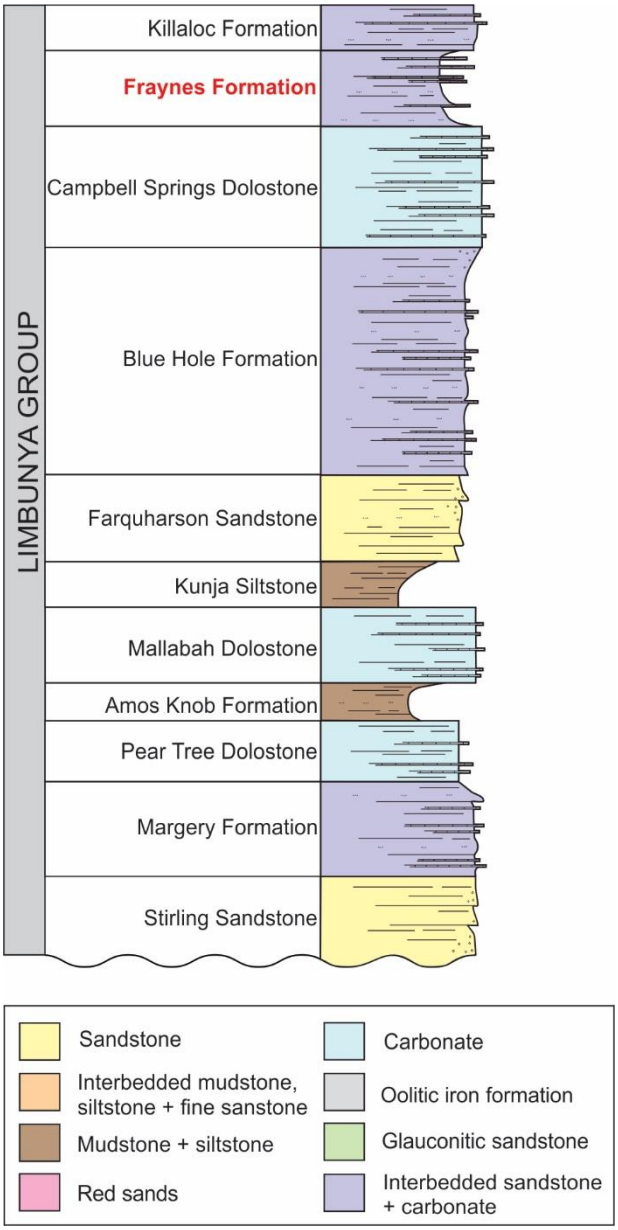

Figure 8: Stratigraphic column of the Limbunya Group from the Birrindudu Basin, including the carbonate rich Fraynes Formation, which is investigated here. Note that thickness indicated here are representative only. Adapted from Ahmad and Munson (2013) and Munson (2014).

3. SAMPLES AND METHODS

3.1 Coorong waters

Near-surface and groundwater samples were collected from the Coorong lagoon system in South Australia (Figure 5 and Appendix A). Coordinates were obtained at each sampling site using a ProDSS handheld multi-parameter meter, which was also used for

on-site measurements of physical and chemical water properties including the dissolved oxygen content, salinity and pH.

3.1.1 NITROGEN WATER AND PARTICULATE ANALYSIS

Water samples (50 mL volumes) collected in pre-acid cleaned HDPE bottles were filtrated using Millex 0.2 μm PTFE syringe filters immediately upon collection, to halt any microbial processes and associated pH and redox changes. Filtered water samples were then kept on ice during transport, and later stored in a cold room to further minimise any microbial activity, before elemental and isotope analyses at Monash University, Melbourne.

The full methodology for nitrogen analysis of waters and particulate matter can be found in Appendix B. Briefly, concentrations of NO_3^-, NO_2^- and NH_4^+ were acquired via spectrophotometric analysis using a Lachat QuikChem 8000 Flow Injection Analyzer (FIA) following standard operating procedures (APHA, 2005).

Analysed N isotope compositions are expressed in the conventional delta $\delta^{15}N$ notation, measured in per mil (‰) and calculated based on Equation 1, where the international standard of atmospheric N_2 was used for the normalisation of sample measurements.

$$\delta^{15}N = \left(\frac{(^{15}N / ^{14}N)_{sample}}{(^{15}N / ^{14}N)_{standard}} - 1 \right) \times 1000$$

Equation 1: Delta notation used to express deviations in the ratio of the two stable isotopes of nitrogen ($^{15}N/^{14}N$), comparing samples to an international standard, and with values reported in per mil (‰). The standard used for comparison is atmospheric N_2 (AIR), which has a $\delta^{15}N$ value of 0‰ and a $^{15}N/^{14}N$ ratio of 0.36765 ± 0.00081 (Sigman et al., 2009).

For nitrate and ammonium, $\delta^{15}N$ values were determined by first converting each species to N_2O, before isotope analysis was conducted using a Sercon Hydra 20-22

Continuous Flow Isotope Mass Spectrometer (CF-IRMS) (Wong et al., 2018; Zhang, Altabet, Wu, & Hadas, 2007). International standards including USGS-25, USGS-32, IAEA-N1 and IAEA-NO_3, among others, were run alongside samples to ensure that errors were minimal.

For $\delta^{15}N$ measurements in PON, aliquots of unfiltered water samples were passed separately through PALL Type A/E glass fibre filters with a 1 µm pore size. The filters with trapped PON were sent to Monash University for N isotope analysis, where incubations with acid traps were performed before $\delta^{15}N$ analysis via CF-IRMS (Russell, Wong, & Cook, 2018).

3.1.2 CHROMIUM WATER ANALYSIS

Pre-cleaned HDPE bottles were used to collect 1 L of water at each site, with collected waters immediately stored on ice during transport, and subsequently filtered at the University of Adelaide with the aid of a pump. Initially, GVS Magna nylon membrane filters with a 0.45 µm pore size were used, before Sartorius cellulose nitrate filters of the same size were found to more effectively filter the waters.

Chromium concentrations and isotopic compositions were analysed at the University of Adelaide, using a Phoenix Thermal Ionisation Mass Spectrometer (TIMS), based on work by Bruggman (2018), Toledo (2018) and Farkaš et al. (2018). At least one procedural blank and one standard of JDo-1 dolomite were run with each batch of 12 samples on average, to confirm accuracy and check for possible Cr contamination. The full methods for sample preparation, column chemistry and analysis of Cr are detailed in Appendix C.

Briefly, the filtered water samples were initially evaporated on a hot plate in pre-cleaned 1 L PTFE jars. A sufficient amount of ^{50}Cr-^{54}Cr double spike, prepared at the Czech Geological Survey in Prague (Farkaš et al., 2013), was then added to dried samples, aiming for an estimated "sample to spike" Cr mass ratio of 4:1, before re-drying. The addition of double spike allowed for later corrections of any instrumental and/or procedural Cr isotope fractionation, as well as subsequent determination of sample Cr concentrations and isotope compositions using offline correction algorithms (for details see Farkaš et al. 2013). Aqua regia (a mixture of concentrated HNO_3 and HCl) was then used to re-dissolve samples and ensure homogenisation of Cr from the sample with the spike, before samples were processed through column chromatography.

Chromium was purified or isolated from the sample matrix using a three column chemistry procedure. Briefly, Milli-Q water (MQ) was added to double spiked and evaporated samples to create a solution, before adding ammonium persulphate solution (ADPS) and 1M HCl. Samples were then boiled for approximately 1 hour to oxidise Cr(III) to Cr(VI). Meanwhile, the first anion column was loaded with anion-exchange resin (Bio-Rad AG 1-8X; 100-200 mesh) and pre-cleaned following the standard procedure (Bruggman, 2018; Toledo, 2018). Once cool, the sample solution consisting of spiked Cr(VI) was passed through this column to remove matrix cations and trace elements, and Cr was reductively eluted from the resin using a combination of acids, including 1M HCl and 2M HNO_3. This eluent was again dried down on a hot plate overnight.

A second anion column was required for the complex water samples, with fresh resin pre-cleaned as before. The dried sample was brought back to solution and re-oxidised.

This solution was passed over the column using different acids (see Appendix C for full details), and the eluent was evaporated overnight.

The third column was used to remove any remaining interfering cations from samples. The columns were loaded with cation-exchange resin (Bio-Rad AG 50W-8X; 200-400 mesh) and pre-cleaned with acid, and the final purification and collection of Cr required another distinct set of acids and separation protocols detailed in Appendix C.

Upon collection from the third column and prior to Cr isotope analysis, the purified Cr fractions were dried down, and then loaded onto tungsten (W) filaments using Nb_2O_5 emitter and 2M HNO_3. These filaments with Cr samples were then loaded into the Phoenix IsoProbe TIMS, equipped with six Faraday Collectors. This array allowed simultaneous collection of all four Cr beams (^{50}Cr, ^{52}Cr, ^{53}Cr and ^{54}Cr), as well as ^{51}V to monitor potential interference of ^{50}V on ^{50}Cr, and ^{56}Fe to monitor potential interference of ^{54}Fe on ^{54}Cr.

After tuning to maximise the ^{52}Cr signal intensity, each sample was run at an intensity of ~1V, provided that yields after column chemistry were high enough. Each measurement consisted of 200 cycles at ~4 seconds each, unless they expired sooner. Standards of NIST SRM 979 were run alongside to determine instrumental accuracy. The reported Cr isotope compositions are expressed in the conventional $\delta^{53}Cr$ notation, measured in per mil (‰) and calculated based on Equation 2, where the international standard of NIST SRM 979 was used for normalisation of measured Cr isotope compositions.

$$\delta^{53}Cr = \left(\frac{(^{53}Cr / ^{52}Cr)_{sample}}{(^{53}Cr / ^{52}Cr)_{standard}} - 1 \right) \times 1000$$

Equation 2: Delta notation used to express deviations in the ratio of the two stable isotopes of chromium ($^{53}Cr/^{52}Cr$), comparing samples to an international standard, and with values reported in per mil (‰). The certified standard used for comparison is NIST SRM 979, a chromium nitrate, which has a $\delta^{53}Cr$ value of 0‰ (Paulukat et al., 2016).

Total procedural blanks contained 6 ng of Cr or less, representing only 0.6% of Cr originating from each sample. Therefore, the blank contribution for our $\delta^{53}Cr$ measurements was negligible.

3.2 Greater McArthur Basin shales

Samples of organic-rich shales were selected from the Velkerri, Mainoru and Barney Creek Formations (see Appendix A for details) to cover a wide range of previously determined $\delta^{15}N$ values (Shannon, 2018), to allow assessment of relationships with $\delta^{53}Cr$, and hence plausible redox-controlled coupling between N and Cr isotopes in the McArthur Basin. The sample set was supplemented by the selection of organic-rich shales from the Fraynes Formation (i.e. the correlative equivalent of the Barney Creek Formation), to further test if the observed relationships between $\delta^{15}N$ and $\delta^{53}Cr$ data could be observed in neighbouring basins.

All shale samples had been collected during previous studies (Bullen, 2017; Shannon, 2018), with all, but those from the Mainoru Formation, already finely powdered. Therefore, only Mainoru Formation samples required crushing, using a Rocklabs tungsten carbide (WC) ring mill to avoid possible metal contamination during sample preparation, as stainless steel could be problematic for Cr isotope work. To avoid cross-contamination during milling, all components were cleaned between samples using pure quartz, high pressure air and ethanol.

3.2.1 NITROGEN SHALE ANALYSIS

Most shales samples had pre-existing nitrogen concentration and $\delta^{15}N$ data from prior work by Shannon (2018). However, newly crushed samples from the Mainoru Formation were re-analysed to avoid possible issues of sample non-homogeneity. Powdered samples (~50 mg) were weighed and sealed in Euro Vector pressed tin capsules. These capsules were loaded and run through the Euro Elemental Analyzer (EA) at the University of Adelaide, by combusting samples at temperatures of 1030°C, to produce sample-derived N gasses, which were passed through the Nu-Horizon Isotope Ratio Mass Spectrometer (IRMS) to measure the bulk shale $\delta^{15}N$ values. In-house standards of glycine, glutamic acid and Triphenyl Amine (TPA) were used to monitor instrumental drift and overall performance of the N isotope analyses (see Appendix D).

3.2.2 MAJOR AND TRACE ELEMENT ANALYSIS

Elemental analysis (including approximate Cr concentrations) of acid-digested shales was performed at the University of Adelaide, using an Agilent 8900 Triple Quad Inductively Coupled Plasma Mass Spectrometer (ICP-MS) attached to an Agilent SPS 4 Autosampler at Adelaide Microscopy. Typical external errors on elemental concentration measurements were ~3% (see Shao et al., 2018).

For digestion, powdered samples were leached for 3 hours in 50 mL Cornig CentriStar tubes using 20 mL of 0.5M HCl, agitating frequently. Leached samples were then centrifuged and the leachate was pipetted off before being dried on a hot plate overnight. Dilutions of 1:1000 were completed by adding 2% HNO_3, with a total of 4 mL of liquid analysed for each sample. A calibration curve was established using 5

dilutions of in-house standards ranging 0-500 ppb, with procedural and analytical blanks also run alongside.

3.2.3 CHROMIUM SHALE ANALYSIS

Concentrations and isotopic compositions of Cr in shales were determined at the University of Adelaide using a TIMS instrument, following the approaches detailed in Appendix C, based on modified procedures of Birte Frank (2019) and Toledo (2018).

Aliquots of homogenised shale powders were first placed into clean quartz crucibles, aiming for masses to give a total 1 μg of Cr in each sample. Samples were then ashed in a furnace at 750°C for 5 hours, incinerating any organic phases present.

After cooling, samples were transferred into 50 mL tubes and leached as detailed in Section 3.2.2, before the leachate was centrifuged and filtered to minimise possible contributions from detrital and clay components of the bulk sample. This purification was achieved using Thermo Fisher Scientific PTFE filters with a 0.45 μm pore size, attached to 10 mL Luer syringes. Double spike and aqua regia was then added to the dried eluents as for the water samples, before re-drying.

As for the waters, shale samples were brought back to solution and oxidised by boiling with ADPS. Shale samples were then subjected to a slightly varied three column chemistry to the approach described in Section 3.1.2, where the first column was the second anion column from the water chromatography procedure.

The second column also diverged from the method used for waters, with anion resin and a different selection of acids used to remove excess Fe from the shales (see Appendix C

and Toledo (2018). The eluent or purified Cr fractions were then evaporated overnight, before samples were passed through the third and final cation exchange column as discussed and used previously for water samples.

The Cr fractions purified from ashed and leached shale samples were analysed via TIMS and the double spiking procedure, following the same approach as described in Section 3.1.2.

4. OBSERVATIONS AND RESULTS

Detailed results with measured N and Cr concentrations and isotopic compositions for both water and shale samples are reported in Appendix D, with sections below illustrating the overall trends and variabilities observed.

4.1 Coorong waters

4.1.1 AQUEOUS AND PARTICULATE NITROGEN CONCENTRATIONS AND ISOTOPE DATA

A total of 14 near-surface water samples collected from the Coorong lagoon system (Figure 5) were analysed for ammonium (NH_4^+) concentrations, which ranged from below detection limit (0.001 mg/L) for sample C5sth up to high values of 5.35 mg/L for sample C7. Table 3 below lists this information as well as some other key results, while Figure 9 illustrates how these characteristics vary as a function of sampling latitude. Ammonium concentrations were too low in 6 samples to allow reliable $\delta^{15}N\text{-}NH_4^+$ analyses, but measurements from samples with detectable levels ranged from -3.7‰ for sample C5m to extremely high $\delta^{15}N\text{-}NH_4^+$ values in the South Lagoon, with up to 58.7‰ for sample C9 (see also Figure 10).

Table 3: Summary of nitrogen concentration and isotopic composition results for analyses conducted at Monash University, on waters sampled from the Coorong lagoon and surrounding regions. Full results, including the longitude of sampling sites, pH of waters, NO_3^- concentrations and NO_2^- concentrations, are detailed in Appendix D. Samples labelled <LOD indicate where nitrogen concentrations were below the limit of detection (0.001 mg/L), and N/A indicates where no samples were collected to be analysed. Results are illustrated in Figures 9, 10 and 11 below.

Sample ID	Latitude (°S)	Water Type	Salinity (psu)	Dissolved Oxygen (mg/L)	NH_4^+ (mg-N/L)	$\delta^{15}N$-NH_4^+ (‰)	NO_x (mg-N/L)	PON (mg)	$\delta^{15}N$-PON (‰)
RM	35.28643	River	0.14	6.49	0.0433	<LOD	0.116	N/A	N/A
LL	35.51257	Lake	0.47	8.25	0.0171	<LOD	0.0175	N/A	N/A
C1	35.63015	North Lagoon	30.05	15.6	0.0189	<LOD	<LOD	N/A	N/A
C2	35.69576	North Lagoon	37.24	11.82	0.0334	<LOD	<LOD	N/A	N/A
C3	35.77025	North Lagoon	56.88	10.82	0.595	2.5	<LOD	N/A	N/A
C4	35.78586	North Lagoon	66.21	12.34	1.69	2.1	<LOD	N/A	N/A
C5	35.90234	Lagoon	83.79	9.26	3.795	2.7	<LOD	0.115	4.85
C5m	35.902758	Lagoon	79.83	6.63	3.28	-3.7	<LOD	0.2	5.23
C5sth	35.890239	Lagoon	196.64	2.53	<LOD	<LOD	<LOD	0.18	7.90
C7	35.93762	South Lagoon	105.78	10.44	5.35	53.9	<LOD	0.14	5.37
C8	36.060425	South Lagoon	99.25	6.16	2.56	58.5	<LOD	0.15	4.70
C9	36.15948	South Lagoon	100.43	9.99	4.31	58.7	<LOD	0.24	4.50
SC	36.1278	Creek	14.55	4.61	0.49	6.3	0.0153	N/A	N/A
SW	36.293955	Ocean	36.13	8.31	0.000811	<LOD	<LOD	N/A	N/A

In total, 3 lagoon water samples had highly fractionated $\delta^{15}N$-NH_4^+ values above 50‰, well above typical expectations for natural surface waters. As such, these analyses were repeated 3 times to ensure accuracy, with similar results obtained each time. Interestingly, unlike the early morning lagoon water sample of C5m, which yielded a negative $\delta^{15}N$-NH_4^+ value, the day-time equivalent of C5 gave a much heavier $\delta^{15}N$-NH_4^+ value of 2.7‰ (Figure 10), documenting significant daily variation.

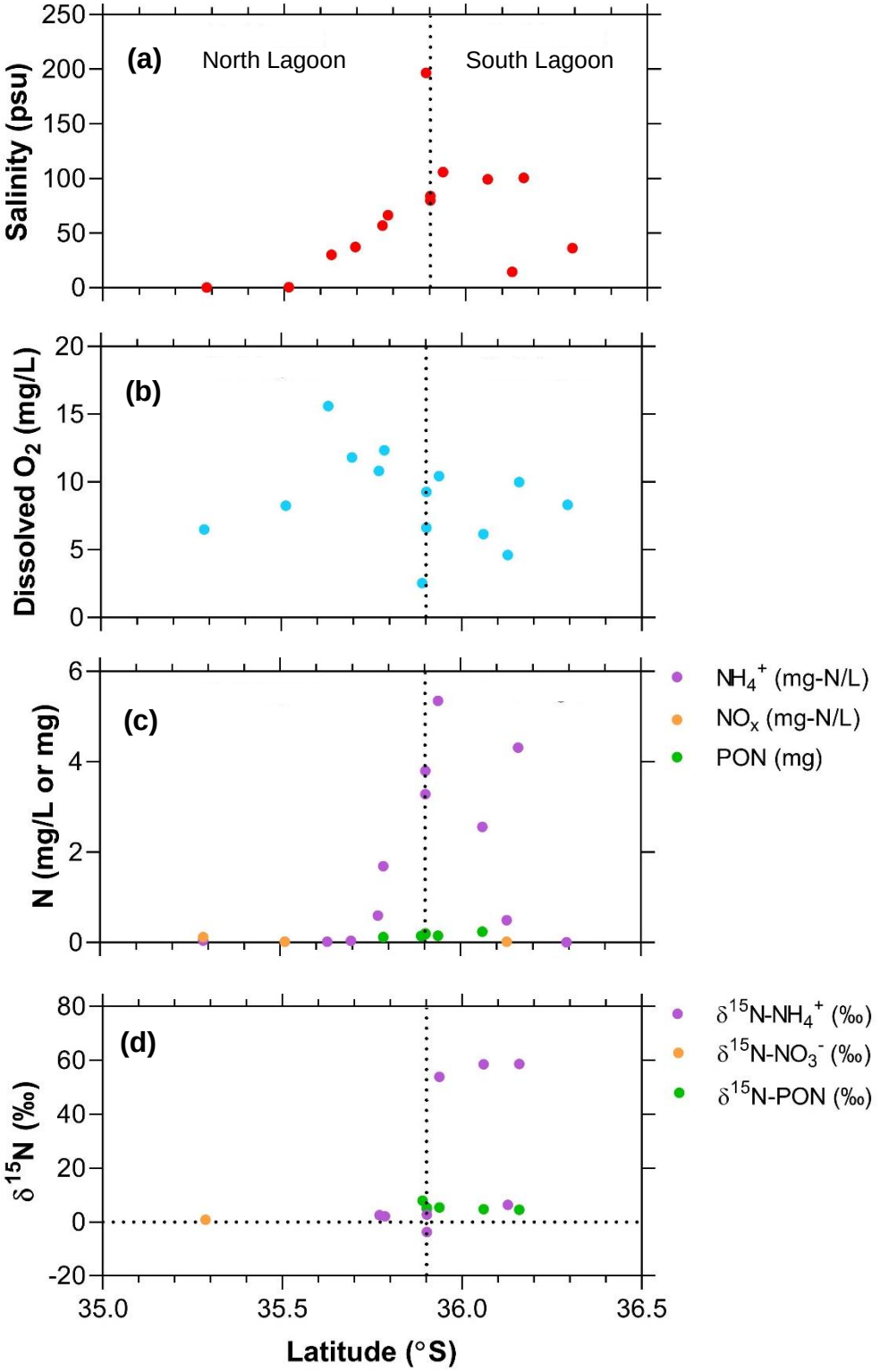

Figure 9: Summary of water characteristics and nitrogen results from waters sampled from the Coorong lagoon and surrounding regions, plotted against the latitude of sampling sites. (a) Salinity profile. (b) Dissolved oxygen content. (c) Concentration of nitrogen as ammonium, nitrogen oxides or particulate organic matter. (d) Isotopic composition of ammonium, nitrate and particulate organic matter.

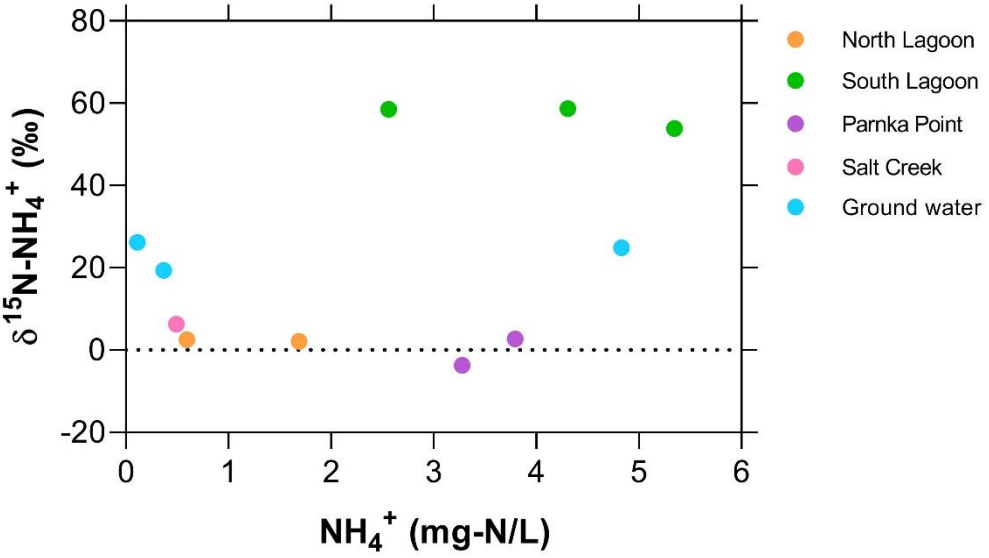

Figure 10: Concentration and isotopic composition of ammonium in surface waters (orange, green, purple and pink) and groundwaters (blue) from regions around the Coorong lagoon. Note that Salt Creek, an input into the southern end of the Coorong, displays similar behaviour to samples from the South Lagoon.

Nitrogen oxide (NO_x i.e. NO_2^- + NO_3^-) concentrations were high enough to be measured in only 3 water samples (see Table 3). In these waters, concentrations of NO_3^- ranged from 0.00643 mg/L for SC (Salt Creek) to 0.11482 mg/L for RM (River Murray), while all lagoon waters were below detection limits. The only sample with a high enough NO_3^- concentration to allow N isotopic analysis was also RM, which yielded a δ^{15}N-NO_3^- value of 0.8‰.

Analysis of PON from filtered waters was undertaken on 6 samples from Parnka Point and the South Lagoon (see Table 3 and Figure 11). The PON contents ranged from 0.09 mg to 0.27 mg of N per filter, however, these values are not an accurate representation of concentration due to the uneven distribution of particles on each filter. Multiple filters were used for some samples due to varying filtration difficulty, so averages of the δ^{15}N-PON for each site was taken. These isotopic compositions ranged from a δ^{15}N of 4.5‰ for C9 to 7.9‰ for C5sth.

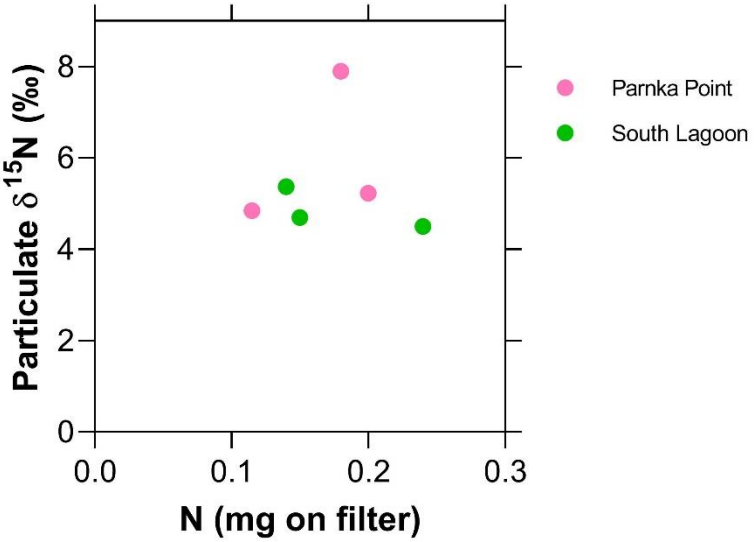

Figure 11: Concentration and isotopic composition of particulate organic nitrogen (PON) in water samples from Parnka Point (pink) and the South Lagoon (green). Values shown are averages from between 1 and 3 filters used for each sample.

4.1.2 AQUEOUS CHROMIUM CONCENTRATIONS AND ISOTOPE DATA

Unfortunately, due to difficulties with separation and purification of Cr from the complex and saline lagoon waters, with very low concentrations, δ^{53}Cr values obtained were of poor accuracy and precision (Table 4). Only one value for sample C3 (North Lagoon) was deemed as useable, yielding a δ^{53}Cr of 0.565 ± 0.123‰. Nevertheless, all other δ^{53}Cr data, although of poor quality, displayed positive fractionation. Approximate concentrations were also obtained via isotope dilution (based on double spike analysis), displaying a range from 0.48 ppb for sample C2 (North Lagoon) up to 34.79 ppb of Cr for SC.

Table 4: Chromium concentrations and isotopic composition of water samples from the Coorong lagoon and surrounding regions, calculated via a TIMS instrument and double spike analysis. Samples labelled N/A indicates where analyses were not able to be conducted. Errors shown are based on the standard deviation of measurements obtained through TIMS analysis.

Sample ID	Latitude (°S)	Water Type	δ^{53}Cr (‰)	δ^{53}Cr error (‰)	Cr (ppm)
RM	35.28643	River	N/A	N/A	0.00316
LL	35.51257	Lake	N/A	N/A	N/A
C1	35.63015	North Lagoon	N/A	N/A	0.00056
C2	35.69576	North Lagoon	N/A	N/A	0.00048
C3	35.77025	North Lagoon	0.565	0.123	0.00120
C4	35.78586	North Lagoon	N/A	N/A	N/A
C5	35.90234	Lagoon	3.792	0.776	0.00068
C5m	35.902758	Lagoon	N/A	N/A	0.00093
C5sth	35.890239	Lagoon	1.168	0.289	0.00122
C7	35.93762	South Lagoon	0.830	0.26	0.00063
C8	36.060425	South Lagoon	1.414	0.458	0.00586
C9	36.15948	South Lagoon	N/A	N/A	N/A
SC	36.1278	Creek	2.265	3.206	0.03479
SW	36.293955	Ocean	N/A	N/A	N/A

4.2 Greater McArthur Basin shales

4.2.1. NITROGEN CONCENTRATIONS AND ISOTOPIC COMPOSITION OF BULK SHALES

Pre-exiting nitrogen data came from 18 organic-rich shale samples from the Velkerri, Fraynes, and Barney Creek Formations (Shannon, 2018). Additional N concentration and δ^{15}N data were collected for 6 shales samples from the Mainoru Formation (all data in Appendix D). The range of values for each formation are summarised in Table 5 below, with the Barney Creek Formation yielding the lowest N concentrations but the highest δ^{15}N values. A cross-plot of all N concentrations and δ^{15}N values is presented below in Figure 12.

Table 5: Summary of the maximum and minimum nitrogen concentrations and $\delta^{15}N$ values for bulk shales from the greater McArthur Basin, as measured by IRMS at the University of Adelaide.

Formation	Min N Concentration (%)	Max N Concentration (%)	Min $\delta^{15}N$ (‰)	Min $\delta^{15}N$ (‰)
Velkerri	0.06	0.24	0.79 ± 0.14	1.97 ± 0.05
Mainoru	0.03	0.07	3.95 ± 0.15	5.65 ± 0.08
Fraynes	0.07	0.14	4.64 ± 0.08	6.58 ± 0.08
Barney Creek	0.01	0.03	6.23 ± 0.18	8.37 ± 0.18

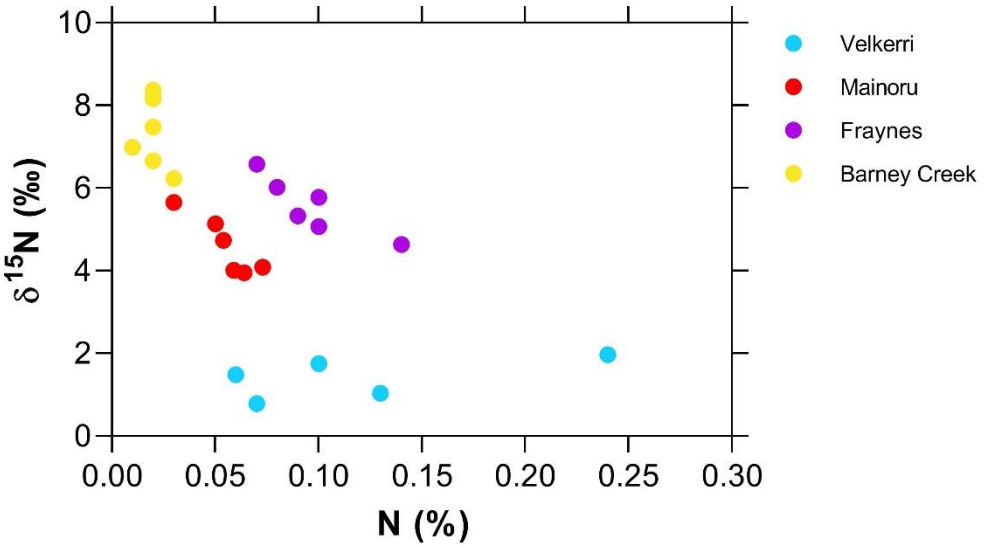

Figure 12: Concentration and isotopic composition of total nitrogen in bulk shale samples collected from several formations within the greater McArthur Basin, from the older Fraynes and Barney Creek Formations with typically higher $\delta^{15}N$ values, to the younger Velkerri Formation with less fractionated $\delta^{15}N$ values. Error bars are not shown as they are smaller than the size of data points.

4.2.2. MAJOR AND TRACE ELEMENT DATA

A suite of 55 major and trace elements, including Cr and rare earth elements (REE), were analysed by ICP-MS from leached shale samples (see Appendix D). Cr concentrations determined in this way allowed more accurate double spiking of shale samples, but the Cr concentrations presented in Figure 13 are from more accurate and precise double spike determination via TIMS analyses.

4.2.3. CHROMIUM CONCENTRATIONS AND ISOTOPIC COMPOSITION OF LEACHED SHALES

Chromium concentrations and isotope compositions, measured by the TIMS and double spike method, were analysed for 24 shale samples from the greater McArthur Basin. Additional samples were run, but accurate results could not be obtained due to low concentrations, or poor Cr signal intensities, and are hence not presented here. The range of values determined by TIMS are summarised below in Table 6, with all data plotted in Figure 13.

Table 6: Summary of the maximum and minimum chromium concentrations and δ^{53}Cr values for leached shales from the greater McArthur Basin, as measured by TIMS and the double spiking method at the University of Adelaide. Errors shown are based on the standard deviation of measurements obtained through TIMS analysis.

Formation	Min Cr Concentration (%)	Max Cr Concentration (%)	Min δ^{53}Cr (‰)	Min δ^{53}Cr (‰)
Velkerri	1.1	38.6	-0.223 ± 0.056	+0.972 ± 0.251
Mainoru	0.9	8.9	-0.100 ± 0.046	+0.527 ± 0.045
Fraynes	3.9	49.7	-0.265 ± 0.117	+0.469 ± 0.135
Barney Creek	14.4	65.1	-0.264 ± 0.079	-0.106 ± 0.069

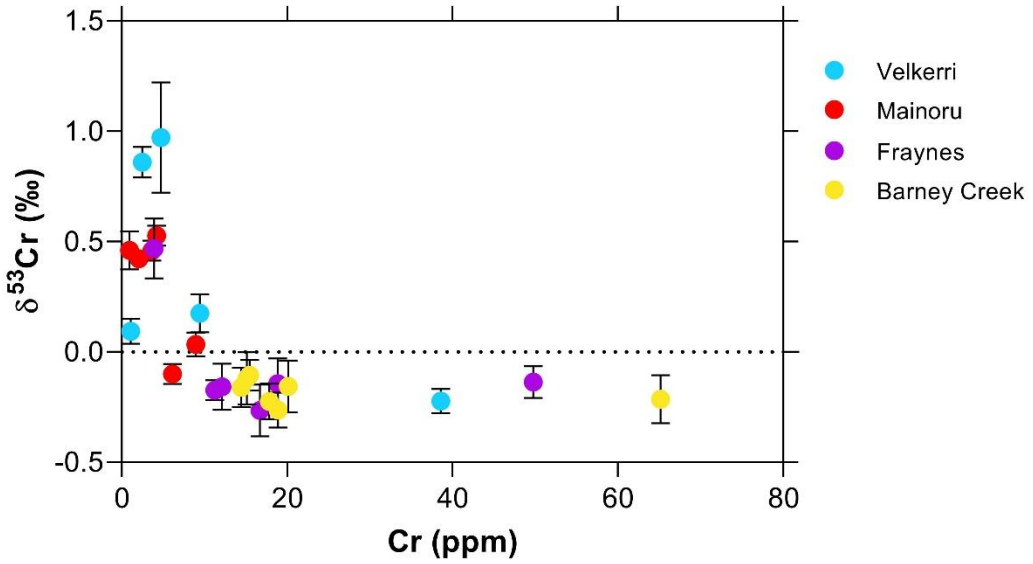

Figure 13: Concentration and isotopic composition of chromium in shale samples from several formations within the greater McArthur Basin, from the younger Velkerri Formation to the older Barney Creek and Fraynes Formations. Error bars show the standard deviation of each cycle from analysis on the TIMS, and are smaller than the data point where not visible.

5. DISCUSSION

5.1 Coorong waters

As no reliable $\delta^{53}Cr$ values could be measured with acceptable accuracy in the complex and hypersaline lagoon waters, comparisons of possible redox-controlled isotope fractionation effects could not be made with $\delta^{15}N$ data collected. Therefore, each element and its isotope variability through the Coorong will be discussed separately in the sections below.

5.1.1. AQUEOUS NITROGEN CYCLING

Before interpreting $\delta^{15}N$ data in terms of internal cycling, it must first be evaluated whether the large N isotope variation observed across the North and South Lagoons (spanning almost 60‰, see Figure 9) is caused by external processes or inputs of anomalous N sources into the lagoon, for example by inputs of N-rich fertilisers from nearby agricultural regions. However, published data of such anthropogenic nitrogen sources, including organic (manure) and inorganic (synthetic) fertilisers, typically carry less fractionated signatures (Chen et al., 2019), ranging from -7 to +3‰ (Michener & Lajtha, 2007).

In the Coorong system, Salt Creek (a stream south of Parnka Point) receives run-off from nearby agricultural regions and provides the South Lagoon's main input of relatively fresh waters. Its $\delta^{15}N\text{-}NH_4^+$ value of 6.3‰ (Figure 10) is fairly close to the maximum range for typical fertilisers, although slightly higher than the majority of published data.

Additionally, the N isotope signatures of groundwater samples yielded $\delta^{15}N\text{-}NH_4^+$ values scatter around 25‰ (Figure 10), which do not overlap with the expected range from fertilisers. These groundwaters were collected from wells near the South Lagoon, so their relatively high $\delta^{15}N\text{-}NH_4^+$ values thus likely reflect the mixing of ammonium sourced from isotopically light freshwaters (~6‰) and the extremely positively fractionated sources of ammonium located in the South Lagoon (up to 59‰).

Considering that the $\delta^{15}N\text{-}NH_4^+$ values of South Lagoon waters are so extreme, and plot away from local sources, it can be concluded that observed N isotope variability in Coorong lagoon waters primarily results from internal processes and local N cycling, rather than being a product of simple mixing of external N sources.

Interestingly, contrary to what is typically expected for relatively oxic but restricted coastal systems such as this, there is a distinct lack of NO_x species within the Coorong lagoon, and a dominance of reduced N species such as NH_4^+ and PON (Figure 9). Two processes that could explain this lack of oxidised N species are microbial redox processes such as dissimilatory nitrate reduction (DNRA), and/or biological assimilation and consumption of NO_x species, leading to the production of PON (Roberts, Kessler, Grace, & Cook, 2014) (Table 1). Although plausible, the above explanations also need to be interpreted in terms of observed extremely high $\delta^{15}N\text{-}NH_4^+$ values.

As indicated above, $\delta^{15}N\text{-}NH_4^+$ results from the South Lagoon show extremely positive and fractionated values of up to 58.7‰, which are to our knowledge the highest reported $\delta^{15}N$ values for natural waters in the Southern Hemisphere, with only one study from an estuary system in Belgium recording a more extreme value of 70.1‰ (De

Brabandere et al., 2007). This study explained these extremely fractionated δ^{15}N-NH_4^+ values by increased biological consumption of ammonium during spring and summer blooms. To test if a similar process can explain the observed South Lagoon results, a Rayleigh modelling approach can be adopted to simulate the expected evolution of δ^{15}N-NH_4^+ values due to such biological consumption, or production of PON from local NH_4^+ sources (see trends in Figure 14 and calculations in Appendix E). This model assumes an open system with a steady reaction rate, with NH_4^+ as the reactant and PON as the product (Equation 3), and an associated isotope fractionation factor of 18.4‰ (see Table 1 and De Brabandere et al., 2007).

The Rayleigh fractionation model used in this study is based on the following equation:

$$\delta^{15}\mathrm{N}_{\mathrm{reactant}} = \delta^{15}\mathrm{N}_{\mathrm{initial}} + \varepsilon(1 - f)$$

Equation 3: Rayleigh equation to calculate δ^{15}N, where ε is the kinetic isotope effect of the transformation and defined as $\varepsilon \approx \delta^{15}N_{product} - \delta^{15}N_{reactant}$ and f is the fraction of reactant remaining, or the unreacted ammonium (Sigman, Karsh, & Casciotti, 2009). Values used for the kinetic isotope effect were ε = 18.4‰ for biological consumption (De Brabandere, Brion, Elskens, Baeyens, & Dehairs, 2007), ε = 30‰ for DNRA (Casciotti, 2016) and ε = 45‰ for volatilisation (Stüeken, Kipp, Koehler, & Buick, 2016)

Notably, the expected product of PON is abundant in the Coorong lagoon waters (Figure 11), so it seems plausible that biological uptake could explain the extreme isotopic fractionation. However, the simulated δ^{15}N-NH_4^+ trend (green line in Figure 14) never reaches such high δ^{15}N-NH_4^+ values of about 59‰, as measured in South Lagoon samples, confirming that biological consumption alone cannot be used to explain results. Similarly, while DNRA can be used to explain the enrichments of NH_4^+, the isotopic fractionation modelled for this process (orange line in Figure 14) is also not sufficient to explain the extremely fractionated δ^{15}N-NH_4^+ values in the South Lagoon.

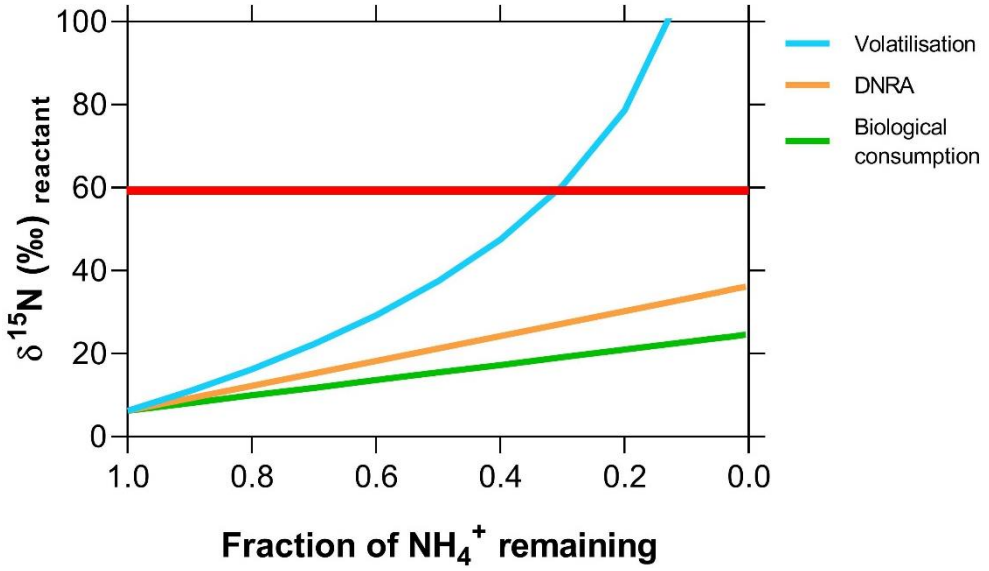

Figure 14: Rayleigh or steady-state fractionation models for δ^{15}N-NH_4^+. The bottom curve uses ε = 18.4‰ and models biological consumption (De Brabandere et al., 2007). The middle curve uses ε = 30‰ as the upper limit to average fractionations observed for DNRA (Casciotti, 2016). The top curve uses ε = 45‰, the maximum value for volatilisation (Stüeken et al., 2016). This is the only model that reaches δ^{15}N-NH_4^+ values as high as those observed in the South Lagoon, approximately marked by the horizontal red bar. These models assume an input from Salt Creek, using the NH_4^+ value of 6.3‰ as $\delta^{15}N_{initial}$, although a lower value of ~2-3‰ using the North Lagoon as the input could also be used, and still results in large enough fractionations. Numbers for each model are outlined in Appendix E.

Importantly, the volatilisation of ammonium to ammonia is associated with the larger isotopic effect of up to 45‰ (see Table 1 and Stüeken et al., 2016). Therefore, this inorganic process linked to evaporation, which is expected to be dominant during warm and drought-affected seasons (Webster, 2010), could explain the observed extremely fractionated δ^{15}N-NH_4^+ values in the South Lagoon (blue line in Figure 14). Further, the Coorong is becoming increasingly hyper-saline due to evaporation and minimal input of fresh water through barrages (Shao et al., 2018), with predominantly alkaline waters (pH ~7-9). This alkalinity in turn provides an ideal environment for the conversion of ammonium to ammonia, and hence volatilisation of isotopically light NH_3 gas from the

system (see Figure 15). This process will thus leave the remaining NH_4^+ pool in the lagoon enriched in heavy N isotopes (Stüeken, Buick, & Schauer, 2015).

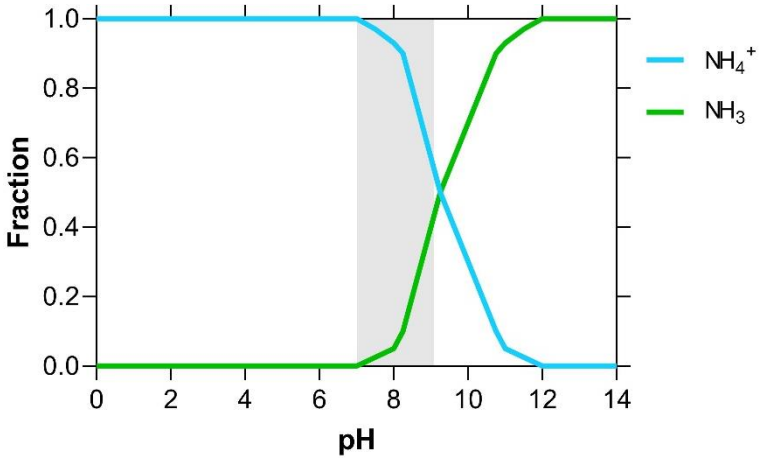

Figure 15: Effect of pH on the relative proportions of aqueous ammonium (NH_4^+) and volatile ammonia (NH_3) at a constant temperature of 25°C. The shaded grey region indicates the range of pH values recorded in the Coorong lagoon and surrounds, between approximately a pH of 7 and 9. This range of values is associated with the pH-dependent transformation between ammonium and ammonia, helping to explain the volatilisation of NH_3 occurring in samples from the South Lagoon. Adapted from (Stüeken et al., 2015).

This NH_3 volatilisation may not be sufficient to explain the lack of NO_x and high abundance of NH_4^+ in local lagoon waters, and therefore DNRA could still be considered to explain the change and abundances of the observed N species. Additionally, a combination of the two isotopic effects (i.e. volatilisation and DNRA) would also allow for larger isotopic fractionations to be observed, while more NH_4^+ remains in the South Lagoon.

Finally, one negative $\delta^{15}N\text{-}NH_4^+$ value is observed for the early morning lagoon water sample at Parnka Point (Figure 10). This diurnal variation could be explained by the shutdown of photosynthetic and biological activity overnight, as well as the lack of evaporation and an increase in the amount of reductive processes occurring.

5.1.2. AQUEOUS CHROMIUM CYCLING

Due to analytical challenges with Cr isotope measurements of Cr-poor hypersaline lagoon waters with complex matrix, the generated data are of poor accuracy and limited quality. This shortcoming must be accounted for when any comparisons or interpretations of data are made. Nevertheless, in general, the limited Cr isotope data display positive isotope fractionations (Table 4), suggesting input of waters with high δ^{53}Cr values from the River Murray and/or Southern Ocean (Frei et al., 2009; Rickli, Janssen, Hassler, Ellwood, & Jaccard, 2019), or alternatively active Mn-catalysed redox cycling of Cr within the lagoon (Miletto et al., 2019).

5.2 Greater McArthur Basin shales

To test if chromium isotopes co-vary with nitrogen isotopes as a function of local biologically-driven redox cycling (see Gueguen et al., 2016; Moos, 2018), isotopes of these elements measured in shales can be plotted against each other, as in Figure 16.

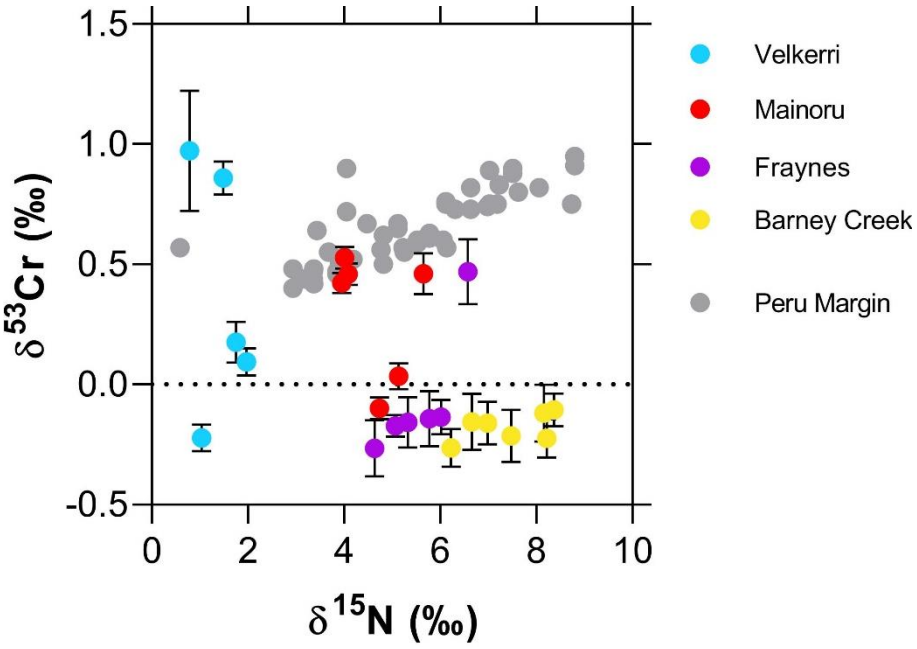

Figure 16: Cross-plot of $\delta^{15}N$ and $\delta^{53}Cr$ values for organic-rich shale samples from several formations within the greater McArthur Basin. Error bars for $\delta^{15}N$ are smaller than the data points and not visible. The older Fraynes and Barney Creek Formations tend to show lower $\delta^{53}Cr$ and higher $\delta^{15}N$ values, while the younger Velkerri Formation shows an opposite relationship. A negative relationship is observed between these isotopes, contrary to previous studies (Gueguen et al., 2016; Moos, 2018). The $\delta^{15}N$ and $\delta^{53}Cr$ values of leached sediments from the Peru Margin study by Gueguen et al. (2016) are shown in grey for comparison of the trends observed.

Previous studies have demonstrated a positive correlation between $\delta^{15}N$ and $\delta^{53}Cr$ in both seawaters and recent marine sediments from the OMZ (Oxygen Minimum Zone) (see Figure 2), explained by microbially-mediated redox changes in the local environments (Moos, 2018), and by glacial/interglacial redox changes linked to biological productivity (Gueguen et al., 2016). Interestingly, this positive co-variance of $\delta^{15}N$ and $\delta^{53}Cr$ data is not observed in shales from the greater McArthur Basin, which instead suggest an opposite trend (Figure 16) and possible negative correlation (R^2 = 0.3). This disagreement with published data therefore suggests that microbial redox processes are likely not the primary driving mechanisms for the isotope fractionation trends observed in these greater McArthur Basin systems. As such, each isotope system and trends observed will be discussed and interpreted separately in the sections below.

5.2.1. NITROGEN RECORD IN BULK SHALES

Nitrogen isotope variations measured in shales from the McArthur Basin (Figure 12) exhibit a systematic long-term trend over ca. 300 Ma, where $\delta^{15}N$ data evolve from more positive values at ca. 1.64 Ga (Barney Creek and Fraynes Formations) to less positive signatures in younger samples at 1.31 Ga (Velkerri Formation), with an overall large temporal change in $\delta^{15}N$ of about 6‰ (Figure 17).

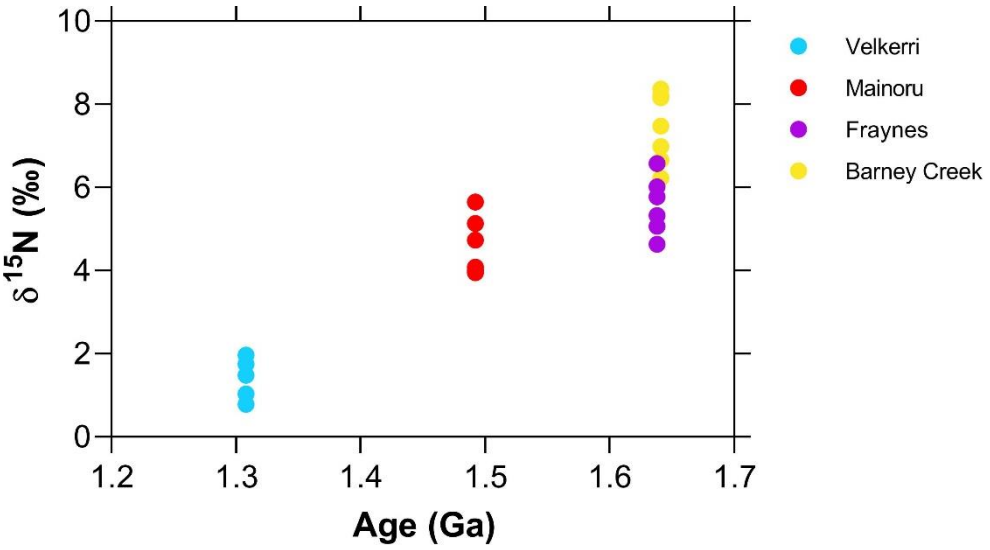

Figure 17: Variation of $\delta^{15}N$ values with time for shales from the greater McArthur Basin, with approximate ages shown for each formation. The Fraynes and Barney Creek Formations are interpreted as time equivalents, but have been offset here for clearer visualisation of results. Error bars are smaller than the size of data points. A general trend to lower $\delta^{15}N$ values is noted in younger samples.

This shift in $\delta^{15}N$ values could be explained via Rayleigh fractionation effects in the possibly semi-restricted and redox-stratified McArthur Basin, similarly to the situation discussed previously for nitrogen isotope data in the Coorong lagoon, where an excess of reduced N species and volatilisation of NH_3, with an associated large isotopic fractionation, can cause high $\delta^{15}N$ values. Importantly, NH_3 volatilisation will only occurs in alkaline settings with high evaporation rates (Stüeken et al., 2015). These conditions are expected during deposition of carbonate-rich facies, such as the older

Barney Creek and Fraynes Formations (Figures 7 and 8), making them suitable for volatilisation and the associated N isotope fractionation. Gypsum needles preserved in slightly younger rocks of the McArthur Group further point to evaporation, likely in a restricted costal lagoon setting (Schmid, 2015) much like the modern Coorong.

Comparatively, the younger sediments from the Mainoru and Velkerri Formations are richer in sandstone and mudstone (Figure 7), typically formed under more "acidic" conditions (due to the lack of marine carbonate phases). These siliciclastic settings would thus be less conductive to NH_3 volatilisation, preventing the generation of large N isotope fractionations, which is consistent with the lower $\delta^{15}N$ values measured in these younger shales.

Seawater evaporation or volatilisation of gases would, of course, not affect chromium isotope fractionation in this same way, as Cr is a heavy metal not present in gaseous form in typical low-temperature marine environments. Therefore, no correlation would be expected between $\delta^{53}Cr$ and $\delta^{15}N$ data in marine shales if volatilisation of NH_3 was the main driver, rather than microbial N and Cr redox processes.

5.2.2 CHROMIUM RECORD IN LEACHED SHALES

Before interpreting $\delta^{53}Cr$ values, confirmation that Cr isotope signals are predominantly from an authigenic (and not detrital) component of sediments is required. As aluminium (Al) is enriched in clays and silicates, and essentially absent in well-preserved marine carbonates, the Al/Cr ratio can be used as a proxy to assess detrital contamination in marine archives such as shales (Gilleaudeau et al., 2016). No statistically significant

relationship is observed in these elemental concentrations (Figure 18), confirming the Cr analysed was primarily from the authigenic-shale component, and not detrital phases.

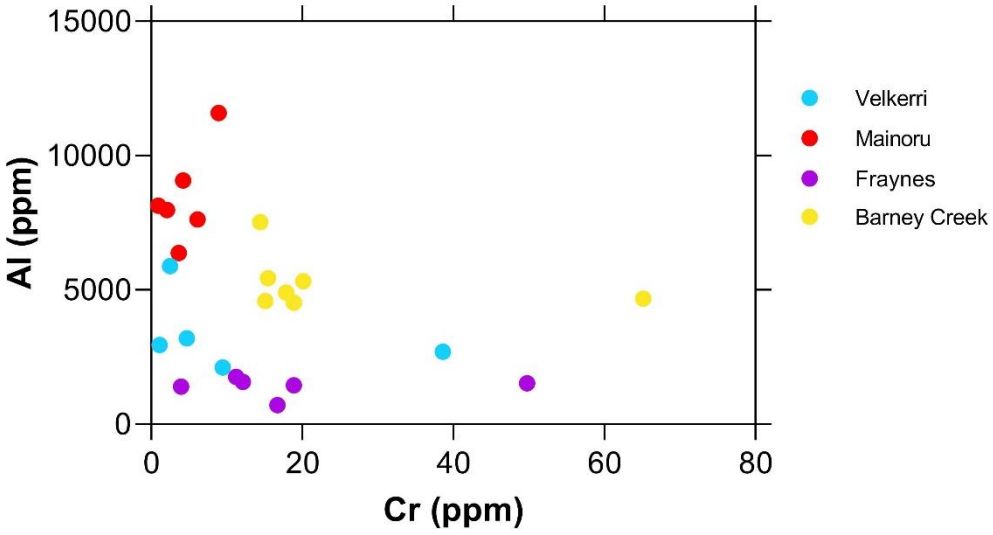

Figure 18: Cross plot of Cr and Al concentrations in samples from several formations in the greater McArthur Basin, each calculated from TIMS and ICP-MS analysis respectively and both measured in ppm. No correlation is observed, indicating that the Cr analysed was from the authigenic component of sediments, rather the detrital component.

In-situ microbial manganese oxidation of Cr has recently been proposed as a cause of changes in δ^{53}Cr values within the water column and marine sediments (Miletto et al., 2019). This concept suggests that Cr can experience isotopic fractionation away from the influence of oxidative continental weathering (Frei et al., 2009). However, δ^{53}Cr values from the studied shales exhibit no obvious trend with Mn concentrations (Figure 19), suggesting that this is not the case for the studied sample set.

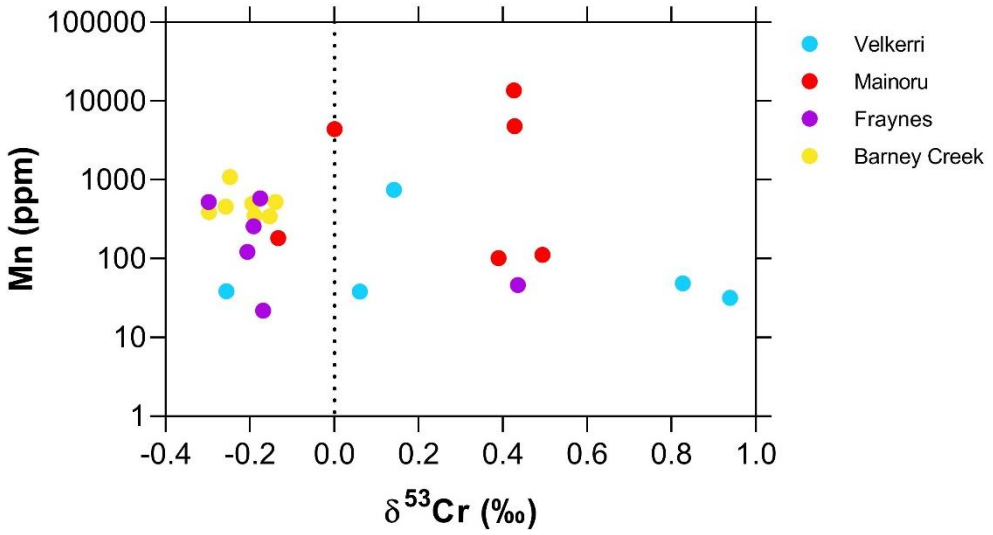

Figure 19: Cross plot of δ^{53}Cr values and Mn concentrations in samples from formations within the greater McArthur Basin. To show all values, the axis of Mn concentrations has been displayed in the logarithmic scale. No obvious trend is observed between δ^{53}Cr values and Mn concentrations, suggesting that in-situ microbial Mn reduction of Cr has not affected the isotopic values.

While there is a great deal of variation in δ^{53}Cr values measured, particularly within the younger Velkerri Formation, a general temporal trend towards more positive values in younger samples is noted (Figure 20). With a variable but progressively increasing abundance of oxygen in the ocean-atmosphere system over time (Lyons et al., 2014), it is expected that more oxic conditions would be associated with geologically younger samples, which is also supported by our data. Younger shales from the McArthur Basin show more positively fractionated Cr isotope values, indicative of oxidative continental weathering (Frei et al., 2009).

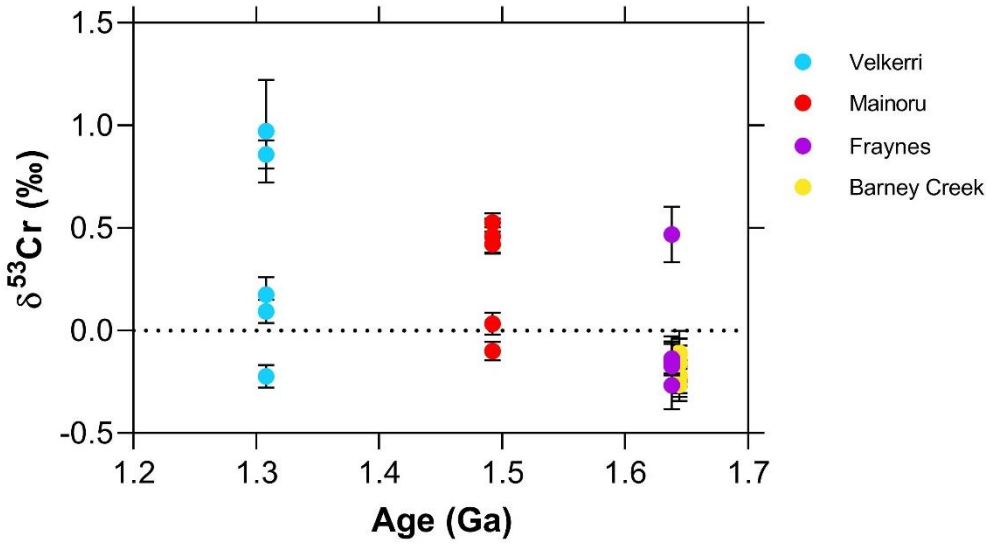

Figure 20: Variation of $\delta^{53}Cr$ values with time for shales from the greater McArthur Basin, with approximate ages shown for each formation. The Fraynes and Barney Creek Formations are interpreted as time equivalents, but have been offset here for clearer visualisation of results. A range of $\delta^{53}Cr$ values are observed, although a general trend towards more positive fractionations is noted in younger samples, such as the Velkerri Formation

To further explore how marine redox conditions, and thus oxygen levels, may have varied through this time (i.e. from 1.64 to 1.31 Ga), another proxy can be examined. Cerium (Ce) is an effective palaeo-redox proxy in marine settings as, similarly to Cr, it exists in two redox states. Anomalies of this element are expressed as Ce/Ce*, with concentrations of Ce compared to neighbouring rare earth elements, Lanthanum (La) and Praseodymium (Pr), normalised to Post Archean Australian Shale (PAAS) (Tostevin et al., 2016). In consistently oxic waters, Ce(III) is oxidised to Ce(IV), which is less soluble and easily removed from the water column by sorption to hydroxides, resulting in a negative Ce anomaly in marine records (Bau & Dulski, 1996). In contrast, negative Ce/Ce* anomalies will not be observed under anoxic conditions due to the similar chemical properties of La and Pr, resulting in precipitates with similar concentrations of each of these three elements (Wang, Liu, & Schmitt, 1986). However, in redox-stratified waters, both negative and positive Ce anomalies can be observed, driven by iron hydroxide remineralisation across the redoxcline (Elderfield & Greaves,

1981). As such, the observation of Ce anomalies in either direction is indicative of active redox cycling through the water column.

Samples from the greater McArthur Basin mostly fall within the indeterminate range (Figure 21), but both positive and true negative Ce anomalies are observed. These anomalies are explained above by a redox-stratified water column, indicative of an oxygenated water body. Shale samples from the Velkerri Formation with negative Ce/Ce* anomalies demonstrate active oxidative Ce cycling, consistent also with the positive $\delta^{53}Cr$ values measured, because if parts if the water column are oxic, then presumably there is appreciable O_2 in the atmosphere to fractionate Cr. Redox stratification, specifically of the Velkerri Formation, is further supported by other studies, which also display positive and negative Ce anomalies (Cox et al., submitted).

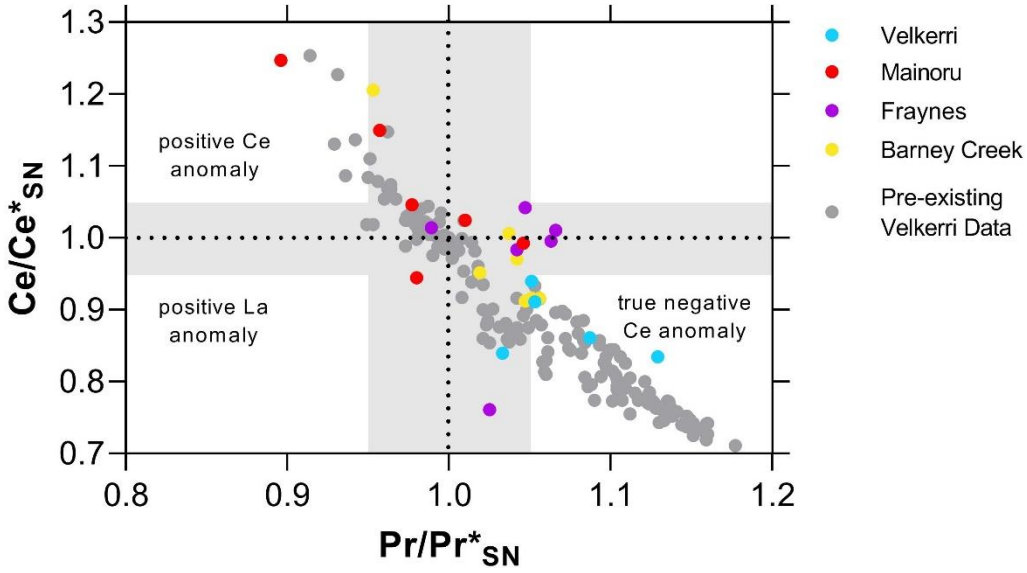

Figure 21: Cross plot of Ce and Pr anomalies in shales from the greater McArthur Basin, based on Bau and Dulski (1996). Cerium anomalies are calculated as $Ce^*_{SN} = \frac{Ce_{SN}}{\sqrt{La_{SN} \times Pr_{SN}}}$, where SN indicates that elemental concentrations in the sample have been normalised to PAAS using values from Nance and Taylor (1976). Praseodymium anomalies are calculated similarly as $Pr^*_{SN} = \frac{Pr_{SN}}{\sqrt{Ce_{SN} \times Nd_{SN}}}$. The dotted lines indicate concentrations expected for PAAS, with the grey region indicating values that are indeterminate. Positive Ce anomalies suggest anoxic conditions, while true negative Ce anomalies suggest oxic conditions. Data previously collected from the Velkerri Formation is also shown in grey, providing further evidence that this depositional system was redox stratified (Cox et al., submitted).

The Velkerri Formations presents the greatest evidence for oxia (see Figure 21), and has $\delta^{53}Cr$ values of up to +0.97‰. With a temporal increase in $\delta^{53}Cr$ values in shale samples over geological time (Figure 20), accompanied by a decrease in Cr concentrations (Figure 13), the fractionation associated with Cr(VI) reduction can be approximated via Rayleigh fractionation models (Equation 4) (Bruggman, 2018) to address the conditions needed to obtain these high $\delta^{53}Cr$ values (see trends in Figure 22 and calculations in Appendix E).

In such a model, a starting $\delta^{53}Cr$ value of 0‰ can be assumed for Cr(VI) dissolved in McArthur Basin palaeo-seawater (close to igneous or unfractionated Cr reservoirs, see Figure 4) (Bauer et al., 2018), while different Cr fractionation factors can be used depending on what is believed to be the dominant process. These factors include -0.8‰, the value typically accepted for Cr(VI) reduction in homogenous oceans worldwide (Scheiderich et al., 2015). However, this may differ in restricted regions, where local Cr cycling can dominate (Farkaš et al., 2018). Values in semi-restricted basins tend to fall off this Rayleigh line, indicating the significance of local factors such as freshwater influx and seasonal variations in primary productivity (Paulukat et al., 2016). Therefore, other fractionation factors to explore include -3.11‰, a value reported for reduction by organic reductants (Kitchen et al., 2012), or even $\alpha = 0.9985$, from the combined effect of reduction by aqueous Cr(VI) followed by Fe(II) (Døssing et al., 2011).

The corresponding $\delta^{53}Cr$ signature of remaining (unreacted) Cr(VI) pool can be then calculated based on the following Rayleigh equation:

$$\delta^{53}Cr_{unreacted} = [(\delta^{53}Cr_{initial} + 10^3)\, f^{(\alpha-1)}] - 10^3$$

Equation 4: Rayleigh equation used to calculate $\delta^{53}Cr$, where *f* is the fraction of reactant (Cr(VI)) remaining and α is the instantaneous fractionation factor for the reduction of Cr(VI) to Cr(III). The α value is defined as $\alpha \approx R_{prod} - R_{react}$, where R_{prod} and R_{react} are the $^{53}Cr/^{52}Cr$ ratios of the instantaneously reduced Cr and that in the reactant (Cr(VI)) pool, respectively (Ellis, Johnson, & Bullen, 2002). Alternately, α can be defined as α = (ε /1000) + 1 where ε is the kinetic isotope effect (Bauer et al., 2018). Fractionation factors used in this study are ε = -0.8‰ for homogenous oceans worldwide (Scheiderich, Amini, Holmden, & Francois, 2015), ε = -3.11‰ for reduction by organic reductants (Kitchen, Johnson, Bullen, Zhu, & Raddatz, 2012) α = 0.9985 for reduction by aqueous Cr(VI) followed by Fe(II) (Døssing, Dideriksen, Stipp, & Frei, 2011).

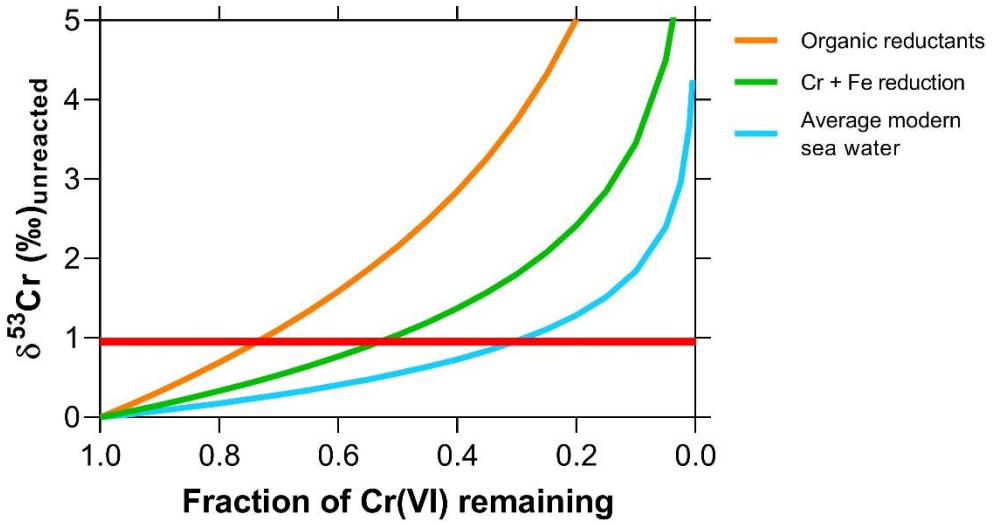

Figure 22: Rayleigh fractionation model for $\delta^{53}Cr$. The lower curve uses ε = -0.8‰, the value typically accepted for modern oceans worldwide (Scheiderich et al., 2015). The upper curve uses ε = -3.11‰, a value reported for reduction by organic reductants (Kitchen et al., 2012). The middle curve comparatively uses α = 0.9985, interpreted to be from the combined effect of homogenous reduction by aqueous Cr(VI) followed by the reduction of intercalated Cr(VI) by Fe(II) (Døssing et al., 2011). All three models can reach the maximum fractionations observed in greater McArthur Basin samples, indicated approximately by the horizontal red bar. These models all assume a $\delta^{53}Cr_{initial}$ value of 0‰ for simplicity, although continental run-off and surface water can have different isotopic values (Bauer et al., 2018). The numbers associated with each model are outlined in Appendix E.

In these presented models (Figure 22) three different fractionation factors (or reduction pathways) for the removal of oxic Cr(VI) from seawater are explored, but all can produce the higher or most positively fractionated δ^{53}Cr values observed in the studied shale samples.

As the McArthur Basin samples come from a range of formations (i.e., carbonate or sandstone associated shales) and represent a large time frame of more than 300 Ma, no single Cr fractionation factor or redox process can be deemed as the most representative or plausible. However, regardless of the mechanisms for Cr oxidation and reduction, all support the existence of oxidised Cr(VI) in waters of the McArthur Basin, subsequent partial back reduction of this Cr(VI) to Cr(III) and associated positive isotopic fractionations (Figure 20).

A number of negative δ^{53}Cr values are also documented through these samples, and can either reflect a complementary and isotopically light Cr(III) reservoir, produced during reduction of Cr(VI), or alternatively increased reductive activity during the back-reduction of Cr(VI) to Cr(III), associated with more anoxic waters (Bruggman, 2018). As most of these negative or less fractionated Cr isotope values occur within the older Barney Creek and Fraynes Formations, a generally more reducing local marine environment with limited dissolved oxygen is supported during deposition of the older shales, compared to the younger counterparts that likely formed in relatively more oxic settings.

6. CONCLUSIONS

Using water samples from the modern Coorong as well as Proterozoic-aged organic-rich shales from the greater McArthur Basin, the cause for shifts in $\delta^{15}N$ and $\delta^{53}Cr$ values has been investigated. An enrichment of reduced nitrogen species with large $\delta^{15}N\text{-}NH_4^+$ values are found in waters from the Coorong lagoon, with extremely heavy $\delta^{15}N\text{-}NH_4^+$ values (up to 59‰) documented in the South Lagoon. The enrichment of NH_4^+ is proposed to have been driven by DNRA, with subsequent volatilisation of NH_3 in alkaline waters causing the large isotopic fractionations. Chromium isotopes from the Coorong were, however, of inadequate quality as the hypersaline waters were generally Cr-poor with a complex matrix, and thus analytically challenging, so the relationship between $\delta^{15}N$ and $\delta^{53}Cr$ could not be tested in this setting. Nevertheless, the generally positive Cr isotope values in lagoon waters support either the input of freshwaters with high $\delta^{53}Cr$ values from the River Murray and/or Southern Ocean, or active redox cycling of Cr within the lagoon.

In contrast, both $\delta^{15}N$ and $\delta^{53}Cr$ values were obtained from organic-rich sedimentary rocks deposited in the greater McArthur Basin between approximately 1.64 and 1.31 Ga. Interestingly, these do not display the positive co-variation between Cr and N isotopes observed recently in other studies (Gueguen et al., 2016; Moos, 2018), so the hypothesis that shifts in marine $\delta^{53}Cr$ records are the result of biologically-mediated N redox processes is proven false in this instance. Rather, N fractionation is proposed to be linked to the “lithology”, or carbonate chemistry, and pH of depositional systems. Older organic-rich samples displaying more positive $\delta^{15}N$ values are associated with carbonate-rich and evaporitic facies formed under presumably more “alkaline” conditions, where volatilisation of NH_3 and thus N isotope fractionation could

efficiently occur (as also observed in the alkaline Coorong lagoon system). Comparatively, younger shales come from more "acidic" or siliciclastic dominated settings (with no carbonates), and display lower $\delta^{15}N$ values. Thus, Cr isotopes do not appear to be affected by biologically-mediated or microbial N cycling, with results alternately supporting $\delta^{53}Cr$ as a proxy for changes in local redox conditions within the Greater McArthur Basin, likely linked to the gradual increase of O_2 levels in the mid-Proterozoic ocean-atmosphere system.

ACKNOWLEDGMENTS

Firstly, I would like to thank the ARC Linkage team for providing the funding that made this project possible. Special thanks go to my supervisor, Dr Juraj Farkas, as well as my co-supervisors Dr Alan Collins and Dr Jonathan Tyler for their guidance and vast knowledge. I would also like to express my gratitude towards Dr Robert Klaebe for all of his assistance with chromium analysis, as well as Dr Sylvie Bruggmann for her assistance. Further thanks go to David Bruce for his support with everything lab related, and to Dr Luke Mosley and Yuexiao Shao for their contributions to work on the Coorong. Additionally, I would like to recognise the fantastic work of Dr Sarah Gilbert from Adelaide Microscopy for elemental analysis, Dr Wei Wen Wong for nitrogen analysis of waters, and Dr Tony Hall and Dr Kristine Nielson for nitrogen analysis of shales. Dr Morgan Blades, Dr Lucy McGee and the Metal Isotope Group have also provided much appreciated encouragement and general guidance. Finally, I would like to thank the honours cohort for their support, valuable insights and great times that we have had together throughout this year, I wish you all the best for the future!

REFERENCES

AHMAD, M., DUNSTER, J. N., & MUNSON, T. J. (2013). Chapter 15: McArthur Basin. In *Geology and mineral resources of the Northern Territory (Special Publication 5)*: Northern Territory Geological Survey.

AHMAD, M., & MUNSON, T. J. (2013). Chapter 17: Birrindudu Basin. In *Geology and mineral resources of the Northern Territory (Special Publication 5)*: Northern Territory Geological Survey.

AMERICAN PUBLIC HEALTH ASSOCIATION, AMERICAN WATER WORKS ASSOCIATION, & WATER ENVIRONMENT FEDERATION. (2005). *Standard methods for the examination of water and wastewater* (21st ed.). Washington D.C.: APHA-AWWA-WEF.

BAIN, D., J., & BULLEN, T., D. (2005). Chromium isotope fractionation during oxidation of Cr(III) by manganese oxides. *Geochim. Cosmochim. Acta, 69*(10), A212-A212.

BAU, M., & DULSKI, P. (1996). Distribution of yttrium and rare-earth elements in the Penge and Kuruman iron-formations, Transvaal Supergroup, South Africa. *Precambrian Research, 79*(1-2), 37-55.

BAUER, K. W., GUEGUEN, B., COLE, D. B., FRANCOIS, R., KALLMEYER, J., PLANAVSKY, N., & CROWE, S. A. (2018). Chromium isotope fractionation in ferruginous sediments. *Geochimica et Cosmochimica Acta, 223*, 198-215. doi:10.1016/j.gca.2017.10.034

BIRTE FRANK, A. (2019). *Chromium isotopes variations in black shales: Evaluating the applicability of chromium stable isotope signatures of ancient black shales as a paleoredox archive.* (Doctor of Philosophy Ph.D. Thesis), University of Copenhagen, Denmark.

BRUGGMAN, S. (2018). *Assessing the potential of the chromium isotope system to record redox changes.* (Doctor of Philosophy Ph.D. Thesis), University of Copenhagen, Denmark.

BULLEN, M. (2017). *Isotopic constraints on the depositional environment and paleo-redox conditions of the greater McArthur Basin, Northern Territory.* (Honours Degree in Geology), The University of Adelaide, Adelaide.

CAMPBELL, I. H., & ALLEN, C. M. (2008). Formation of supercontinents linked to increases in atmospheric oxygen. *Nature Geoscience, 1*(8), 554-558. doi:10.1038/ngeo259

CANFIELD, D. E., ZHANG, S., BIRTE FRANK, A., WANG, X., WANG, H., SU, J., . . . FREI, R. (2018). Highly fractionated chromium isotopes in Mesoproterozoic-aged shales and atmospheric oxygen. *Nature communications, 9*(1), 1-11. doi:10.1038/s41467-018-05263-9

CASCIOTTI, K. L. (2016). Nitrogen and oxygen isotopic studies of the marine nitrogen cycle. *Annual Review of Marine Science, 8*(1), 379-407. doi:10.1146/annurev-marine-010213-135052

CHEN, F., ZHOU, X., LAO, Q., WANG, S., JIN, G., CHEN, C., & ZHU, Q. (2019). Dual isotopic evidence for nitrate sources and active biological transformation in the Northern South China Sea in summer. *PLOS One, 14*(1), E0209287. doi:10.1371/journal.pone.0209287

COX, G. M., COLLINS, A. S., BLADES, M. L., JARRETT, A. J. M., SHANNON, A. V., YANG, B., . . . BARUCH, E. T. (submitted). *A very unconventional hydrocarbon play: The Mesoproterozoic Velkerri Formation of Northern Australia*. AAPG Bulletin.

COX, G. M., SANSJOFRE, P., BLADES, M. L., FARKAS, J., & COLLINS, A. S. (2019). Dynamic interaction between basin redox and the biogeochemical nitrogen cycle in an unconventional Proterozoic petroleum system. *Scientific Reports, 9*(1), 5200. doi:10.1038/s41598-019-40783-4

DE BRABANDERE, L., BRION, N., ELSKENS, M., BAEYENS, W., & DEHAIRS, F. (2007). $\delta^{15}N$ dynamics of ammonium and particulate nitrogen in a temperate eutrophic estuary. *Biogeochemistry, 82*(1), 1-14. doi:10.1007/s10533-006-9047-1

DØSSING, L. N., DIDERIKSEN, K., STIPP, S. L. S., & FREI, R. (2011). Reduction of hexavalent chromium by ferrous iron: A process of chromium isotope fractionation and its relevance to natural environments. *Chemical Geology, 285*(1), 157-166. doi:10.1016/j.chemgeo.2011.04.005

ELDERFIELD, H., & GREAVES, M. J. (1981). Negative cerium anomalies in the rare earth element patterns of oceanic ferromanganese nodules. *Earth and Planetary Science Letters, 55*(1), 163-170. doi:10.1016/0012-821X(81)90095-9

ELLIS, A. S., JOHNSON, T. M., & BULLEN, T. D. (2002). Chromium isotopes and the fate of hexavalent chromium in the environment. *Science (New York, N.Y.), 295*(5562), 2060-2062. doi:10.1126/science.1068368

ELLIS, A. S., JOHNSON, T. M., & BULLEN, T. D. (2004). Using chromium stable isotope ratios to quantify Cr(VI) reduction: Lack of sorption effects. *Environmental science & technology, 38*(13), 3604. doi:10.1021/es0352294

FAKHRAEE, M., HANCISSE, O., CANFIELD, D. E., CROWE, S. A., & KATSEV, S. (2019). Proterozoic seawater sulfate scarcity and the evolution of ocean–atmosphere chemistry. *Nature Geoscience, 12*(5), 375-380. doi:10.1038/s41561-019-0351-5

FARKAŠ, J., CHRASTNY, V., NOVAK, M., CADKOVA, E., PASAVA, J., CHAKRABARTI, R., . . . BULLEN, T. D. (2013). Chromium isotope variations ($\delta^{53}/^{52}$Cr) in mantle-derived sources and their weathering products: Implications for environmental studies and the evolution of $\delta^{53}/^{52}$Cr in the Earth's mantle over geologic time. *Geochimica et Cosmochimica Acta, 123*, 74-92. doi:10.1016/j.gca.2013.08.016

FARKAŠ, J., FRÝDA, J., PAULUKAT, C., HATHORNE, E. C., MATOUŠKOVÁ, Š., ROHOVEC, J., . . . FREI, R. (2018). Chromium isotope fractionation between modern seawater and biogenic carbonates from the Great Barrier Reef, Australia: Implications for the paleo-seawater δ^{53}Cr reconstruction. *Earth and Planetary Science Letters, 498*, 140-151. doi:10.1016/j.epsl.2018.06.032

FREI, R., GAUCHER, C., POULTON, S. W., & CANFIELD, D. E. (2009). Fluctuations in Precambrian atmospheric oxygenation recorded by chromium isotopes. *Nature, 461*(7261), 250-254. doi:10.1038/nature08266

FREI, R., PAULUKAT, C., BRUGGMANN, S., & KLAEBE, R. M. (2018). A systematic look at chromium isotopes in modern shells – Implications for paleo-environmental reconstructions. *Biogeosciences, 15*(16), 4905-4922. doi:10.5194/bg-15-4905-2018

GILLEAUDEAU, G. J., FREI, R., KAUFMAN, A. J., KAH, L. C., AZMY, K., BARTLEY, J. K., . . . KNOLL, A. H. (2016). Oxygenation of the mid-Proterozoic atmosphere: Clues from chromium isotopes in carbonates. *Geochemical Perspectives Letters, 2*(2), 178-187. doi:10.7185/geochemlet.1618

GLIBERT, P. M., MIDDELBURG, J. J., MCCLELLAND, J. W., & VANDER ZANDEN, M. J. (2019). Stable isotope tracers: Enriching our perspectives and questions on sources, fates, rates, and pathways of major elements in aquatic systems. *Limnology and Oceanography, 64*(3), 950-981. doi:10.1002/lno.11087

GUEGUEN, B., REINHARD, C. T., ALGEO, T. J., PETERSON, L. C., NIELSEN, S. G., WANG, X., . . . PLANAVSKY, N. J. (2016). The chromium isotope composition of reducing and oxic marine sediments. *Geochimica et Cosmochimica Acta, 184*, 1-19. doi:10.1016/j.gca.2016.04.004

HAESE, R. R., MURRAY, E. J., & WALLACE, L. (2009). *Nutrient sources, water quality, and biogeochemical processes in the Coorong, South Australia*: Geoscience Australia, Canberra.

HAN, R., QIN, L., BROWN, S. T., CHRISTENSEN, J. N., & BELLER, H. R. (2012). Differential isotopic fractionation during Cr(VI) reduction by an aquifer-derived bacterium under aerobic versus denitrifying conditions. *Applied and environmental microbiology, 78*(7), 2462. doi:10.1128/AEM.07225-11

IZBICKI, J. A., BALL, J. W., BULLEN, T. D., & SUTLEY, S. J. (2008). Chromium, chromium isotopes and selected trace elements, western Mojave Desert, USA. *Applied Geochemistry, 23*(5), 1325-1352. doi:10.1016/j.apgeochem.2007.11.015

JACKSON, M. J., SWEET, I. P., PAGE, R. W., & BRADSHAW, B. E. (1999). The South Nicholson and Roper Groups: Evidence for the early Mesoproterozoic Roper Superbasin. In B. E. Bradshaw & D. L. Scott (Eds.), *Integrated basin analysis of the Isa Superbasin using seismic, well-log, and geopotential data: An evaluation of the economic potential of the northern Lawn Hill Platform* (Vol. 19). Canberra, Australia: Australian Geological Survey Organisation Record.

JAMIESON-HANES, J. H., AMOS, R. T., & BLOWES, D. W. (2012). Reactive transport modeling of chromium isotope fractionation during Cr(VI) reduction. *Environmental science & technology, 46*(24), 13311. doi:10.1021/es3046235

KITCHEN, J. W., JOHNSON, T. M., BULLEN, T. D., ZHU, J., & RADDATZ, A. (2012). Chromium isotope fractionation factors for reduction of Cr(VI) by aqueous Fe(II) and organic molecules. *Geochimica et Cosmochimica Acta, 89*, 190-201. doi:10.1016/j.gca.2012.04.049

KJERFVE, B. (1986). Comparative oceanography of coastal lagoons. In D. A. Wolfe (Ed.), *Estuarine Variability* (pp. 63-81). University of South Carolina, Columbia: Academic Press.

KNOPPERS, B. (1994). Aquatic primary production in coastal lagoons. In B. Kjerfve (Ed.), *Elsevier Oceanography Series* (Vol. 60, pp. 243-286): Elsevier.

KORTH, F., KOCK, A., ARÉVALO-MARTÍNEZ, D. L., & BANGE, H. W. (2019). Hydroxylamine as a potential indicator of nitrification in the open ocean. *Geophysical Research Letters, 46*(4), 2158-2166. doi:10.1029/2018gl080466

LARGE, R. R., MUKHERJEE, I., GREGORY, D., STEADMAN, J., CORKREY, R., & DANYUSHEVSKY, L. V. (2019). Atmosphere oxygen cycling through the Proterozoic and Phanerozoic. *Mineralium Deposita, 54*(4), 485-506. doi:10.1007/s00126-019-00873-9

LYONS, T. W., REINHARD, C. T., & PLANAVSKY, N. J. (2014). The rise of oxygen in Earth's early ocean and atmosphere. *Nature, 506*, 307-315. doi:10.1038/nature13068

MICHENER, R. H., & LAJTHA, K. (2007). *Stable Isotopes in Ecology and Environmental Science* (2nd ed.). Malden, Massachusetts: Blackwell Publishing Ltd.

MILETTO, M., WANG, X. L., PLANAVSKY, N. J., LUTHER, G., W., LYONS, T. W., & TEBO, B. M. (2019). *Active microbial Mn(II) oxidation mediates Cr(III) oxidation and fractionates Cr stable isotopes* Paper presented at the Goldschmidt Conference, Barcelona

MOOS, S. B. (2018). *The marine biogeochemistry of chromium isotopes.* (Doctor of Philosophy Ph.D. Thesis), Massachusetts Institute of Technology and Woods Hole Oceanographic Institution, Massachusetts.

MOSLEY, L., HAMILTON, B., BUSCH, B., HIPSEY, M., & TAYLOR, B. (2017). *Assessment and modelling of the effects of the 2013-2016 Morella Basin releases on Coorong water quality*. Retrieved from South Australia, The University of Adelaide. doi:10.13140/RG.2.2.13630.08005:

MUNSON, T. J. (2014). *Petroleum geology and potential of the onshore Northern Territory, 2014* (Report 22). Retrieved from Darwin, Northern Territory:

MUNSON, T. J. (2019). *Detrital zircon geochronology investigations of the Glyde and Favenc packages: Implications for the geological framework of the greater McArthur Basin, Northern Territory.* Paper presented at the Annual Geoscience Exploration Seminar (AGES), Alice Springs, Northern Territory.

NANCE, W. B., & TAYLOR, S. (1976). Rare earth element patterns and crustal evolution: Australian post-Archean sedimentary rocks. *Geochimica et Cosmochimica Acta, 40*(12), 1539-1551.

OZAKI, K., REINHARD, C. T., & TAJIKA, E. (2019). A sluggish mid-Proterozoic biosphere and its effect on Earth's redox balance. *Geobiology, 17*(1), 3-11. doi:10.1111/gbi.12317

OZE, C., BIRD, D. K., & FENDORF, S. (2007). Genesis of hexavalent chromium from natural sources in soil and groundwater. *Proceedings of the National Academy of Sciences, 104*(16), 6544. doi:10.1073/pnas.0701085104

PAGE, R. W., JACKSON, M. J., & KRASSAY, A. A. (2000). Constraining sequence stratigraphy in north Australian basins: SHRIMP U–Pb zircon geochronology between Mt Isa and McArthur River. *Australian Journal of Earth Sciences, 47*(3), 431-459. doi:10.1046/j.1440-0952.2000.00797.x

PAULUKAT, C., GILLEAUDEAU, G. J., CHERNYAVSKIY, P., & FREI, R. (2016). The Cr-isotope signature of surface seawater - A global perspective. *Chemical Geology, 444*, 101-109. doi:10.1016/j.chemgeo.2016.10.004

PEREIRA, N. S., VOEGELIN, A. R., PAULUKAT, C., SIAL, A. N., FERREIRA, V. P., & FREI, R. (2016). Chromium-isotope signatures in scleractinian corals from the Rocas Atoll, Tropical South Atlantic. *Geobiology, 14*(1), 54-67. doi:10.1111/gbi.12155

PHILLIPS, B., & MULLER, K. (2006). *Ecological character of the Coorong, Lakes Alexandrina and Albert Wetland of international importance*. Adelaide, South Australia: Dept. for Environment and Heritage.

PLANAVSKY, N. J., REINHARD, C. T., WANG, X., THOMSON, D., MCGOLDRICK, P., RAINBIRD, R. H., . . . LYONS, T. W. (2014). Low mid-Proterozoic atmospheric oxygen levels and the delayed rise of animals. *Science, 346*(6209), 635-638. doi:10.1126/science.1258410

RAFIEI, M., & KENNEDY, M. (2019). Weathering in a world without terrestrial life recorded in the Mesoproterozoic Velkerri Formation. *Nature communications, 10*(1), 3448. doi:10.1038/s41467-019-11421-4

RAWLINGS, D. J. (1999). Stratigraphic resolution of a multiphase intracratonic basin system: The McArthur Basin, Northern Australia. *Australian Journal of Earth Sciences, 46*(5), 703-723. doi:10.1046/j.1440-0952.1999.00739.x

REID, R. J., & MOSLEY, L. M. (2016). Comparative contributions of solution geochemistry, microbial metabolism and aquatic photosynthesis to the development of high pH in ephemeral wetlands in South East Australia. *Science of The Total Environment, 542*, 334-343. doi:10.1016/j.scitotenv.2015.10.040

REINHARD, C. T., PLANAVSKY, N. J., OLSON, S. L., LYONS, T. W., & ERWIN, D. H. (2016). Earth's oxygen cycle and the evolution of animal life. *Proceedings of the National Academy of Sciences of the United States, 113*(32), 8933. doi:10.1073/pnas.1521544113

REINHARD, C. T., PLANAVSKY, N. J. G., B. C., OZAKI, K., ROBBINS, L. J., LYONS, T. W., FISCHER, W., . . . KONHAUSER, K. O. (2016). Evolution of the global phosphorus cycle. *Nature, 541*(7637), 386-389. doi:10.1038/nature20772

REMMELZWAAL, S. R. C., DIXON, S., PARKINSON, I. J., SCHMIDT, D. N., MONTEIRO, F. M., SEXTON, P., . . . JAMES, R. H. (2019). Investigating ocean deoxygenation during the PETM through the Cr isotopic signature of foraminifera. *Paleoceanography and Paleoclimatology, 34*(6), 917-929.

RICKLI, J., JANSSEN, D. J., HASSLER, C., ELLWOOD, M. J., & JACCARD, S. L. (2019). Chromium biogeochemistry and stable isotope distribution in the Southern Ocean. *Geochimica et Cosmochimica Acta, 262*, 188-206. doi:10.1016/j.gca.2019.07.033

ROBERTS, K. L., KESSLER, A. J., GRACE, M. R., & COOK, P. L. M. (2014). Increased rates of dissimilatory nitrate reduction to ammonium (DNRA) under oxic conditions in a periodically hypoxic estuary. *Geochimica et Cosmochimica Acta, 133*, 313-324. doi:10.1016/j.gca.2014.02.042

RODLER, A., SANCHEZ-PASTOR, N., FERNANDEZ-DIAZ, L., & FREI, R. (2015). Fractionation behavior of chromium isotopes during coprecipitation with calcium carbonate: Implications for their use as paleoclimatic proxy. *Geochimica et Cosmochimica Acta, 164*, 221.

RUSSELL, D. G., WONG, W. W., & COOK, P. L. M. (2018). Negligible isotopic fractionation of nitrogen within temperate *Zostera* spp. meadows. *Biogeosciences Discussions, 15*(23), 7225-7234. doi:10.5194/bg-2018-154

SAAD, E. M., SUN, J., CHEN, S., BORKIEWICZ, O. J., ZHU, M., DUCKWORTH, O. W., & TANG, Y. (2017). Siderophore and organic acid promoted dissolution and transformation of Cr(III)-Fe(III)-(oxy)hydroxides. *Environmental science & technology, 51*(6), 3223. doi:10.1021/acs.est.6b05408

SCHAUBLE, E., ROSSMAN, G. R., & TAYLOR, H. P. (2004). Theoretical estimates of equilibrium chromium-isotope fractionations. *Chemical Geology, 205*(1), 99-114. doi:10.1016/j.chemgeo.2003.12.015

SCHEIDERICH, K., AMINI, M., HOLMDEN, C., & FRANCOIS, R. (2015). Global variability of chromium isotopes in seawater demonstrated by Pacific, Atlantic, and Arctic Ocean samples. *Earth and Planetary Science Letters, 423*, 87-97. doi:10.1016/j.epsl.2015.04.030

SCHMID, S. (2015). *Sedimentological review of the Barney Creek Formation in drillholes LV09001, BJ2, McA5, McArthur Basin* (0724572961). Retrieved from Darwin, Northern Territory:

SHANNON, A. (2018). *Understanding the complexities of Proterozoic redox using carbon, nitrogen and trace metal composition of organic rich shales.* (Honours Degree in Geology), The University of Adelaide, Adelaide.

SHAO, Y., FARKAŠ, J., HOLMDEN, C., MOSLEY, L., KELL-DUIVESTEIN, I., IZZO, C., . . . GILLANDERS, B. M. (2018). Calcium and strontium isotope systematics in the lagoon-estuarine environments of South Australia: Implications for water source mixing, carbonate fluxes and fish migration. *Geochimica et Cosmochimica Acta, 239*, 90-108. doi:10.1016/j.gca.2018.07.036

SHERIDAN, M., JOHNS, D., & JOHNSON, H. (2018). The stratigraphic architecture, distribution and hydrocarbon potential of the organic rich Kyalla and Velkerri shales of the Upper Roper Group (McArthur Basin). *The APPEA Journal, 58*(2), 858-864. doi:10.1071/ASEG2018abT7_3C

SIGMAN, D., KARSH, K., & CASCIOTTI, K. L. (2009). Ocean process tracers: Nitrogen isotopes in the ocean. In J. H. Steele, Turekian, K. K., and Thorpe, S. A. (Ed.), *Encyclopedia of Ocean Sciences*: Academic Press.

SIKORA, E. R., JOHNSON, T. M., & BULLEN, T. D. (2008). Microbial mass-dependent fractionation of chromium isotopes. *Geochimica et Cosmochimica Acta, 72*(15), 3631-3641. doi:10.1016/j.gca.2008.05.051

STÜEKEN, E. E., BUICK, R., & SCHAUER, A. J. (2015). Nitrogen isotope evidence for alkaline lakes on late Archean continents. *Earth and Planetary Science Letters, 411*, 1-10. doi:10.1016/j.epsl.2014.11.037

STÜEKEN, E. E., KIPP, M. A., KOEHLER, M. C., & BUICK, R. (2016). The evolution of Earth's biogeochemical nitrogen cycle. *Earth-Science Reviews, 160*(C), 220-239. doi:10.1016/j.earscirev.2016.07.007

THOMAZO, C., & PAPINEAU, D. (2013). Biogeochemical cycling of nitrogen on the early earth. *Elements, 9*(5), 345-351. doi:10.2113/gselements.9.5.345

TOLEDO, G. E. (2018). *Chromium isotope constraints on the Mid-Proterozoic redox: Evidence from $\delta^{53}Cr$ of carbonates from the Greater McArthur Basin, Northern Australia.* (Honours Degree in Geology), The University of Adelaide, Adelaide.

TOSTEVIN, R., SHIELDS, G. A., TARBUCK, G. M., HE, T., CLARKSON, M. O., & WOOD, R. A. (2016). Effective use of cerium anomalies as a redox proxy in carbonate-dominated marine settings. *Chemical Geology, 438*(C), 146-162. doi:10.1016/j.chemgeo.2016.06.027

TRIBOVILLARD, N., ALGEO, T. J., LYONS, T., & RIBOULLEAU, A. (2006). Trace metals as paleoredox and paleoproductivity proxies: An update. *Chemical Geology, 232*(1), 12-32. doi:10.1016/j.chemgeo.2006.02.012

WANG, Y. L., LIU, Y. G., & SCHMITT, R. A. (1986). Rare earth element geochemistry of South Atlantic deep sea sediments: Ce anomaly change at ~54 My. *Geochimica et Cosmochimica Acta, 50*(7), 1337-1355. doi:10.1016/0016-7037(86)90310-8

WEBSTER, I. T. (2010). The hydrodynamics and salinity regime of a coastal lagoon – The Coorong, Australia – Seasonal to multi-decadal timescales. *Estuarine, Coastal and Shelf Science, 90*(4), 264-274. doi:10.1016/j.ecss.2010.09.007

WONG, W. W., POTTAGE, J., WARRY, F. Y., REICH, P., ROBERTS, K. L., GRACE, M. R., & COOK, P. L. M. (2018). Stable isotopes of nitrate reveal different nitrogen processing mechanisms in streams across a land use gradient during wet and dry periods. *Biogeosciences, 15*(13), 3953-3965. doi:10.5194/bg-15-3953-2018

YANG, B., COLLINS, A. S., COX, G. M., JARRETT, A. J. M., DENYSZYM, S., BLADES, M. L., . . . GLORIE, S. (in press). *Mesoproterozoic basin geochemistry ties organic carbon enhancement to nutrient flux from a Northern Australian large igneous province*. Basin Research.

YANG, B., SMITH, T. M., COLLINS, A. S., MUNSON, T. J., SCHOEMAKER, B., NICHOLLS, D., . . . GLORIE, S. (2018). Spatial and temporal variation in detrital zircon age provenance of the hydrocarbon-bearing upper Roper Group, Beetaloo Sub-basin, Northern Territory, Australia. *Precambrian Research, 304*, 140-155. doi:10.1016/j.precamres.2017.10.025

ZHANG, L., ALTABET, M. A., WU, T., & HADAS, O. (2007). Sensitive measurement of NH_4^+ $^{15}N/^{14}N$ ($\delta^{15}NH_4^+$) at natural abundance levels in fresh and saltwaters. *Analytical Chemistry, 79*(14), 5297-5303. doi:10.1021/ac070106d

ZINK, S., SCHOENBERG, R., & STAUBWASSER, M. (2010). Isotopic fractionation and reaction kinetics between Cr(III) and Cr(VI) in aqueous media. *Geochimica et Cosmochimica Acta, 74*(20), 5729-5745. doi:10.1016/j.gca.2010.07.015

APPENDIX A: SAMPLE LOCATIONS

Table A1: Locations and time of collection for waters from the Coorong lagoon and surrounding regions in South Australia. Orange, green and pink indicate samples from the North Lagoon, South Lagoon and connection between these regions (Parnka Point) each respectively, while blue represents other nearby areas sampled.

Sample ID	Location	Date	Time	Latitude (°S)	Longitude (°E)
RM	River Murray, Tailem Bend-Wellington	7/03/2019	10:11 AM	35.28643	139.44801
LL	The Lower Lakes connection, Narrung	7/03/2019	11:16 AM	35.51257	139.18811
C1	North Lagoon, Mark Point	7/03/2019	12:11 PM	35.63015	139.08003
C2	North Lagoon, Long Point	7/03/2019	12:50 PM	35.69576	139.16232
C3	North Lagoon, near Rob's Point	7/03/2019	1:53 PM	35.77025	139.2722
C4	North Lagoon, Noonamena	7/03/2019	2:15 PM	35.78586	139.30191
C5	North Lagoon-South Lagoon connection, Parnka Point	7/03/2019	2:57 PM	35.90234	139.3981
C5m	North Lagoon-South Lagoon connection, Parnka Point	8/03/2019	7:53 AM	35.902758	139.449538
C5sth	North Lagoon-South Lagoon connection, Parnka Point South	8/03/2019	8:22 AM	35.890239	139.404471
C7	South Lagoon, Field Rd	7/03/2019	3:50 PM	35.93762	139.48851
C8	South Lagoon, Policeman's Point	8/03/2019	7:04 AM	36.060425	139.593679
C9	South Lagoon, Salt Creek South	8/03/2019	10:58 AM	36.15948	139.6461
SC	South Lagoon, Salt Creek	8/03/2019	10:31 AM	36.1278	139.64934
SW	Southern Ocean, southern end of the Coorong	8/03/2019	12:50 PM	36.293955	139.697777

Table A2: Locations and dates of collection of groundwaters from the Coorong region in South Australia. Orange and green represent the North Lagoon and South Lagoon samples respectively.

Sample ID	Location	Date	Latitude (°S)	Longitude (°E)
GWN	North Lagoon, North of Noonameena	11/04/2019	35.74087	139.2461
GWR	North Lagoon, near Rob's Point	12/04/2019	35.78502	139.3001
GWP	South Lagoon, beach south of Parnka Point	12/04/2019	35.91363	139.4634
GWSW	South Lagoon, near Stony Wells	11/04/2019	35.94868	139.5448
GWWW2	South Lagoon, inland near Woods Well Rd	11/04/2019	35.98766	139.5745
GWWW	South Lagoon, near Woods Well Rd	11/04/2019	35.99415	139.5475
GWWW3	South Lagoon, beach near Woods Well Rd	11/04/2019	35.99416	139.539

Table A3: Locations of the drill holes supplying samples for each formation explored in the greater McArthur Basin. Various sampling intervals were used in each drill hole for this study.

Formation	Drill Hole ID	Sample Depth (m)	Latitude (°S)	Longitude (°E)	Drilling Datum
Velkerri	Altree 2	640.98	15.923645	133.786592	KB
		664.69			
		760.33			
	Marmbulligan 1	214.3	16.199672	134.771861	RT
	Tanumbirini 1	3199	16.399083	134.703833	RT
Mainoru	Urapunga 5	401.5	14.71060	134.42139	(Not supplied)
		439.65			
		487.5			
		563.1			
		597.8			
	Urapunga 6	251.6	14.74189	134.53359	(Not supplied)
Fraynes	Manbulloo S1	722.55	14.927666	132.268424	RT
		781.7			
		783.54			
		784.65			
		789.46			
		865.8			
Barney Creek	GRNT-79-4	153.4	16.991755	136.303041	GDA94
	GRNT-79-7	638	16.902237	136.300303	GDA94
		668.4			
		678			
		792			
		812.6			
		891			

APPENDIX B: EXTENDED NITROGEN METHODS

All analyses of nitrate, nitrite, ammonium and particulate nitrogen concentrations and isotopic compositions were conducted at Monash University in Melbourne.

Nitrate and nitrite from waters

Methods are adapted from Wong et al. (2018). International standards of USGS-32, USGS-34, USGS-35 and IAEA-NO_3^- were run alongside samples to check analytical accuracy.

- Concentrations of NO_3^- and NO_2^- were found by spectrophotometric analysis using a Lachat QuikChem 8000 Flow Injection Analyzer (FIA) following standard operating procedures (APHA, 2005).
- Cadmium reduction was used to convert all the NO_x (i.e. $NO_3^- + NO_2^-$) in samples to NO_2^-.
- Sodium azide was used to convert NO_2^- to N_2O.
- The resultant N_2O was analysed using a Sercon Hydra 20-22 continuous flow isotope mass spectrometer (CF-IRMS) with a Sercon cyrcoprep system, providing a $\delta^{15}N$ value for NO_3^-.

Ammonium from waters

Methods are adapted from Zhang, Altabet, Wu, and Hadas (2007). Standards of USGS-25, USGS-26 and IAEA-N1 were also run alongside samples.

- Concentrations of NH_4^+ was found by spectrophotometric analysis as above.
- Colourimetric determination of NH_4^+ and NO_2^- concentrations was used to establish if sample dilution or removal of excess NO_2^- was required. If so, sulfanilic acid was added to equal 1.5 times the concentration of NO_2^-. This was allowed to react for at least 30 min, before heating in a boiling water bath for 15 min.
- Once cool, 2 mL of BrO^- working solution was added for each 20 mL of sample, and samples were shaken vigorously. This was allowed to react for 30 min at room temperature, allowing oxidation of NH_4^+ to NO_2^-.
- Excess BrO^- was removed by adding 0.4 mL of arsenite.
- The NO_2^- was reduced to N_2O using sodium azide buffered to a pH of 4-5.
- As for nitrate analysis, the resultant N_2O was analysed using CF-IRMS to determine the $\delta^{15}N$ value.

Particulate nitrogen

Methods are adapted from Russell, Wong, and Cook (2018). Standards of USGS-25, USGS-26 and IAEA-N1 were run alongside samples.

- Remaining water from samples C5, C5m, C5sth, C7, C8 and C9 were stored in a fridge at Waite Campus. MQ was used to rinse PALL Type A/E 1 μm glass fiber filters to ensure cleanliness, before samples were passed through these filters.
- Filters were folded in half to trap particulate matter and frozen before express shipment to Monash University.
- Concentrations were found using colourimetric determination.
- Isotopic signatures were determined by performing incubations in 250 mL Schott laboratory bottles, with target NH_4^+ concentrations of between approximately 17.9 and 28.6 μg in a final volume of 100 mL. De-ionised water was used for any required dilutions.
- A subsample of 1 mL was removed from each diffusion bottle prior to the addition of acid traps, to allow for calculation of the NH_4^+ concentrations as per methods above.
- Acid traps were created using 4 mm x 8 mm slices of pre-ashed GF/F paper and acidified using 20 μL of 2.5 M $KHSO_4$. The acidified filter paper was then housed in 10 μm pore size PTFE membranes with a diameter of 47 mm before being crimped shut.
- Prepared acid traps were added to each diffusion bottle along with 0.6 g of MgO, which raised the pH of the solution to approximately 10.
- Incubations were conducted at room temperate for 3 weeks on shaker tables at 135 rpm.
- Acid traps were dried in a desiccator in the presence of concentrated HCl for 3 weeks.
- Once dry, the filter paper was removed from the PTFE membranes and analysed for the $\delta^{15}N$ value using CF-IRMS as described previously.

APPENDIX C: EXTENDED CHROMIUM METHODS

Procedure modified from work by Toledo (2018), with specifications for waters from Bruggman (2018), and for shales from Birte Frank (2019). Both water and shale samples were processed together, however, some steps are unique to either material and were therefore conducted separately (as indicated in the sequential methods detailed below). All analyses of chromium were conducted at the University of Adelaide.

Sample preparation and spiking

WATERS ONLY

- Samples were collected in pre acid-cleaned PTFE containers. They were kept on ice before being stored in a fridge, to halt any microbial processes.
- A pump aided filtration of multiple samples at an increased rate. Initially, GVS Magna 0.45 µm nylon filters were used, before changing to Sartorius 0.45 µm cellulose nitrate filters, as samples were coming out visibly dirty. Filtered samples were collected in clean 500 mL or 1 L PTFE bottles. All filters were first rinsed in nitric acid to decrease the pH and encourage metal cations such as Cr to remain in solution.
- A total of 150-500 mL of river and lagoon water, or 1-2 L of sea water, was evaporated to dryness in clean PTFE containers on a hot plate at 140°C.

SHALES ONLY

- Following ICP-MS analysis, powdered sample was weighed into clean quartz crucibles to equal ~1 µg of Cr.
- Lids were placed on the crucibles and samples were ashed in a furnace for 5 hours at 750°C.
- Ashed samples were tipped into 50 mL Cornig CentriStar tubes, using 0.5M HCl to rinse the sides and ensure the entire sample was collected. The tube was then filled to 20 mL with acid. This was agitated frequently over 3 hours to leach the sample.
- Tubes were centrifuged at 3000-4000 rpm for ~1 hour, or until all powder had settled to the bottom.
- Pre-cleaned 10 mL Luer syringes were attached with a 0.45 µm PTFE filter, before passing through 2M HCl to further minimse any possible contamination of detrital Cr. Clean 5 ml pipettes were used to transfer the leachate into the syringes, where they were passed through the filter and the mass of the total leachate was recorded.

ALL SAMPLES

- Sufficient ^{50}Cr-^{54}Cr double spike, prepared at the Czech Geological Survey in Prague and diluted to 1.03 ppm, was weighed onto Parafilm and added to each sample in an estimated sample to spike Cr ratio of 4:1. The spike mass was accurately recorded.

- Samples were evaporated to dryness on a hot plate.
- Aqua regia was made up freshly as required, and added to samples to ensure homogenisation with the spike. Enough was added to the water samples to completely cover the salty residue left behind, and 2 mL was added to the shale samples. These were capped for a 2-3 hours before evaporating to dryness.
- Milli-Q water (MQ) was added to bring samples back to solution. Approximately 200 mL was added to water samples, and 20 mL was added to shale samples. This was agitated and left to sit for a day.

Column chromatography

INITIAL ANION COLUMN - WATERS ONLY

- 2 mL of 1M HCl was added to solutions. The pH was then measured using test strips. If greater than 3, 1M HCl was added slowly until the pH was ~2.
- Ammonium persulphate (ADPS) solution was prepared by dissolving ~230 mg of ADPS in 5 mL of MQ and shaking vigorously.
- 1 mL of ammonium persulphate solution was added to each sample. Remaining solution was discarded after use.
- Samples were sealed and placed in 5 L glass beakers with water and a clock glass on top, and boiled thoroughly for 1 hour. This allowed oxidation of Cr.

- Meanwhile, the columns were prepared. The Poly-Prep Bio-Rad columns were first rinsed with MQ. Then ~2/3 of settled anion resin (Bio-Rad AG 1-8X; 100-200 mesh) was added onto column stems.
- To increase capacity, yellow cylinders were rinsed with MQ and added to columns.
- To clean the resin, 1 reservoir of MQ was added.
- Added 1 reservoir of 5M HNO_3.
- Added 1 reservoir of MQ.
- Added 1 reservoir of 6M HCl.
- Added 1 reservoir of MQ.
- Added 1 reservoir of 0.1M HCl.

- After boiling, samples were cooled rapidly by running under cold water. The pH was checked using test strips again. If more than 3, 1M HCl was added until ~2.
- Samples were added to the columns as soon as possible after being removed from the water bath, being careful to avoid the salts settled at the bottom.
- To flush, 25 mL 0.1M HCl was added.
- Added 20 mL MQ.
- To collect the sample, pre-cleaned 30 mL PTFE jars were placed under the columns.
- Simultaneously added 1 mL 2M HNO_3 and 3 drops 5% H_2O_2.
- Simultaneously added 5 mL 2M HNO_3 and 7 drops 5% H_2O_2.

- Once all liquid passed through, samples were dried down on a hot plate overnight.
- Discarded used resin. Rinsed columns out with MQ and store sealed with MQ.

ANION COLUMN - ALL SAMPLES

- Water samples were brought back to solution by adding 20 mL of MQ.
- Prepared fresh batch of ADPS solution as described previously.
- Added 0.25 mL or 0.5 mL of ammonium persulphate solution to each shale and water sample respectively, as well as 0.5 mL of 1M HCl. Less solution was added to the shales to help counter later issues of final samples being hydroscopic.
- Closed lids, and boiled for 1 hour in a rack on a hot plate at 140°C to oxidise Cr.
- Cooled samples by partially submerging them in cold water.

- Meanwhile, anion resin was added to columns and cleaned as detailed for the initial anion column with water samples. However, no cylinders were required at this step.
- After cleaning the resin, each sample was added to a column.
- Samples were flushed by adding 10 mL of 0.2M HCl
- Added 2 mL of 2M HCl
- Added ~1/2 reservoir of MQ

- Placed pre-cleaned 15 mL PTFE vials underneath each column.
- Collected samples by simultaneously adding 1 mL of 2M HNO_3 and 3 drops of 5% H_2O_2.
- Waited ~5 mins.
- Simultaneously added 5 mL of 2M HNO_3 and 7 drops of 5% H_2O_2.

- As for the previous anion column procedure, samples were dried down, resin was discarded, and columns were cleaned and stored with MQ.

IRON COLUMN - SHALES ONLY

- Rinsed columns with MQ. Added ~2/3 of settled anion resin.
- To clean, added 1 reservoir of 5M HNO_3.
- Added 1 reservoir of MQ.
- Added 1 reservoir of 0.2M HCl.
- Added 1 reservoir of 6M HCl.
- Added another reservoir of 6M HCl.

- Meanwhile, 1 mL of 6M HCl was added to dried samples and sat in a sonic bath for ~5 min to re-dissolve.
- Added samples to each column, quickly placing same Teflon container back underneath to collect again.
- Added 1 mL of 6M HCl.
- Added 1 mL of 6M HCl.
- Added 1 mL of 6M HCl.
- Added 1 mL of 6M HCl.

- As previously, samples were evaporated overnight, resin was discarded, and columns were stored in MQ.

CATION COLUMN - ALL SAMPLES

- The Evergreen Scientific columns were first rinsed with MQ. Then ~2/3 of settled cation resin (Bio-Rad AG 50W-8X; 200-400 mesh) was added onto column stems.
- To clean the resin, 1 reservoir of MQ was added.
- Added 1 reservoir of 5M HNO_3.
- Added 1 reservoir of MQ.
- Added 1 reservoir of 6M HCl.
- Added 1 reservoir of MQ.
- Added ~1/2 reservoir of 0.5M HCl.

- Meanwhile, the samples were re-dissolved by adding 0.1 mL of 12M HCl and heating on a hot plate at 130°C for ~10 min.
- 2.3 mL of MQ was added to each sample.

- Each sample was held in a 5 mL pipette while the Teflon was rinsed with MQ. The cleaned Teflon was then placed back under the column and the sample was loaded.
- To collect the Cr, 8 mL of 0.5M HCl was added.

- Samples were evaporated to dryness overnight once all liquid had passed through the columns. As before, the resin was discarded and columns were rinsed and stored with MQ.

LOADING ONTO FILAMENTS

- Added 1 µL of Nb_2O_5 emitter to the centre of filaments. Allowed to evaporate to dryness.
- Dissolved each sample in 1.5 µL of 2M HNO_3, then carefully placed this on the centre of the dried emitter. Evaporated for 1-2 hours to allow the liquid to evaporate and shrink, without running down the sides of the filament.
- Fully dried the loaded samples using an Isotopx Filament Loading Unit, by slowly heating towards ~4.0 A.

APPENDIX D: ELEMENTAL AND ISOTOPIC DATA

Coorong nitrogen data

Table A4: Water quality data and average particulate nitrogen characteristics of water samples from the Coorong lagoon region. Particulate nitrogen values are shown as averages from between 1 and 3 filter papers analysed. Orange, green and pink indicate samples from the North Lagoon, South Lagoon and connection between these regions each respectively, while blue represents other nearby areas sampled.

Sample ID	Salinity (psu)	Dissolved oxygen (mg/L)	pH	Particulate N (mg)	Particulate $\delta^{15}N$ (‰)
RM	0.14	6.49	8.27	-	-
LL	0.47	8.25	8.04	-	-
C1	30.05	15.6	8.21	-	-
C2	37.24	11.82	8.15	-	-
C3	56.88	10.82	7.95	-	-
C4	66.21	12.34	8.21	-	-
C5	83.79	9.26	8.2	0.115	4.85
C5m	79.83	6.63	8.33	0.2	5.23
C5sth	196.64	2.53	7.25	0.18	7.90
C7	105.78	10.44	8.06	0.14	5.37
C8	99.25	6.16	8.15	0.15	4.70
C9	100.43	9.99	8.07	0.24	4.50
SC	14.55	4.61	8.58	-	-
SW	36.13	8.31	8.39	-	-

Table A5: Ammonium and nitrogen oxide characteristics of water samples from the Coorong lagoon region. Orange, green and pink indicate samples from the North Lagoon, South Lagoon and connection between these regions each respectively, while blue represents other nearby areas sampled. <LOD indicates concentrations below the detection limit (0.001mg-N/L) and dashes indicate where analyses could not be conducted as concentrations were too low.

Sample ID	NH_4^+ (mg-N/L)	$\delta^{15}N$-NH_4^+ (‰)	NO_x (mg-N/L)	NO_2^- (mg-N/L)	NO_3^- (mg-N/L)	$\delta^{15}N$-NO_3^- (‰)
RM	0.0433	-	0.116	0.00118	0.11482	0.8
LL	0.0171	-	0.0175	0.00112	0.01638	-
C1	0.0189	-	<LOD	<LOD	<LOD	-
C2	0.0334	-	<LOD	<LOD	<LOD	-
C3	0.595	2.5	<LOD	<LOD	<LOD	-
C4	1.69	2.1	<LOD	<LOD	<LOD	-
C5	3.795	2.7	<LOD	<LOD	<LOD	-
C5m	3.28	-3.7	<LOD	<LOD	<LOD	-
C5sth	<LOD	-	<LOD	<LOD	<LOD	-
C7	5.35	53.9	<LOD	<LOD	<LOD	-
C8	2.56	58.5	<LOD	<LOD	<LOD	-
C9	4.31	58.7	<LOD	<LOD	<LOD	-
SC	0.49	6.3	0.0153	0.00887	0.00643	-
SW	0.000811	-	<LOD	<LOD	<LOD	-

Table A6: Ammonium and nitrogen oxide characteristics of groundwater samples from the Coorong lagon region. Orange and green indicate samples from near the North and South Lagoon. <LOD indicates concentrations below the detection limit (0.001mg-N/L) and dashes indicate where analyses could not be conducted as concentrations were too low.

Sample ID	NH_4^+ (mg-N/L)	$\delta^{15}N$-NH_4^+ (‰)	NO_x (mg-N/L)	$\delta^{15}N$-NO_3^- (‰)
GWN	0.01	-	0.24	10.4
GWR	0.02	-	0.01	-
GWP	0.11	26.2	0.03	-
GWSW	4.83	24.9	0.04	-
GWWW2	0.08	-	0.01	-
GWWW	0.01	-	<LOD	-
GWWW3	0.37	19.4	0.01	-

Coorong chromium data

Table A7: Chromium concentrations and isotopic composition of water samples from the Coorong lagoon region. Orange, green and pink indicate samples from the North Lagoon, South Lagoon and connection between these regions each respectively, while blue represents other nearby areas sampled. Dashes indicate where no data was able to be collected.

Sample ID	Location	$\delta^{53}Cr$ (‰)	$\delta^{53}Cr$ error (‰)	Cr (ppm)
RM	River Murray, Tailem Bend-Wellington	-	-	0.00316
C1	North Lagoon, Mark Point	-	-	0.00056
C2	North Lagoon, Long Point	-	-	0.00048
C3	North Lagoon, near Rob's Point	0.565	0.123	0.00120
C5	North Lagoon-South Lagoon connection, Parnka Point	3.792	0.776	0.00068
C5m	North Lagoon-South Lagoon connection, Parnka Point	-	-	0.00093
C5sth	North Lagoon-South Lagoon connection, Parnka Point South	1.168	0.289	0.00122
C7	South Lagoon, Field Rd	0.830	0.26	0.00063
C8	South Lagoon, Policeman's Point	1.414	0.458	0.00586
SC	South Lagoon, Salt Creek	2.265	3.206	0.03479

Greater McArthur Basin nitrogen data

Table A8: Nitrogen concentrations and isotopic composition of shales from the greater McArthur Basin. Blue, red, purple and yellow colouring indicates the Velkerri, Mainoru, Fraynes and Barney Creek Formations respectively.

Drill Hole ID	Sample Depth (m)	$\delta^{15}N$ (‰)	$\delta^{15}N$ error (‰)	N (%)
Altree 2	640.98	1.04	0.03	0.13
Altree 2	664.69	1.75	0.03	0.10
Altree 2	760.33	1.97	0.05	0.24
Marmbulligan 1	214.3	1.49	0.14	0.06
Tanumbirini 1	3199	0.79	0.14	0.07
Urapunga 5	401.5	4.74	0.15	0.054
Urapunga 5	439.65	5.14	0.15	0.050
Urapunga 5	487.5	4.09	0.15	0.073
Urapunga 5	563.1	3.95	0.15	0.064
Urapunga 5	597.8	4.01	0.15	0.059
Urapunga 6	251.4	5.65	0.08	0.030
Manbulloo S1	722.99	4.64	0.08	0.14
Manbulloo S1	781.7	5.78	0.08	0.10
Manbulloo S1	783.54	6.58	0.08	0.07
Manbulloo S1	784.65	5.07	0.08	0.10
Manbulloo S1	789.46	5.33	0.08	0.09
Manbulloo S1	865.8	6.02	0.08	0.08
GRNT-79-4	153.4	6.99	0.18	0.01
GRNT-79-7	657.6	6.86	0.18	0.02
GRNT-79-7	668.4	8.16	0.18	0.02
GRNT-79-7	678	6.23	0.18	0.03
GRNT-79-7	792	8.22	0.18	0.02
GRNT-79-7	812.6	8.37	0.18	0.02
GRNT-79-7	891	7.48	0.18	0.02

In-house standards run alongside the samples listed above in Table A8 were glycine ($\delta^{15}N$ = +1.32‰) and glutamic acid ($\delta^{15}N$ = -6.18‰), as well as the certified reference material for elemental concentrations of Triphenyl Amine (TPA, C:N = 18:1).

Greater McArthur Basin chromium data

Table A9: Chromium concentrations and isotopic composition of shales from the greater McArthur Basin. Blue, red, purple and yellow colouring indicates the Velkerri, Mainoru, Fraynes and Barney Creek Formations respectively

Drill Hole ID	Sample Depth (m)	δ^{53}Cr (‰)	δ^{53}Cr error (‰)	Cr (ppm)
Altree 2	640.98	-0.223	0.056	38.588
Altree 2	664.69	0.175	0.069	2.484
Altree 2	760.33	0.094	0.251	4.708
Marmbulligan 1	214.3	0.860	0.046	6.131
Tanumbirini 1	3199	0.972	0.054	8.932
Urapunga 5	401.5	-0.100	0.045	3.644
Urapunga 5	439.65	0.034	0.045	4.213
Urapunga 5	487.5	0.459	0.086	0.920
Urapunga 5	563.1	0.423	0.117	16.701
Urapunga 5	597.8	0.527	0.115	18.850
Urapunga 6	251.4	0.461	0.135	3.913
Manbulloo S1	722.99	-0.265	0.046	11.235
Manbulloo S1	781.7	-0.143	0.105	12.095
Manbulloo S1	783.54	0.469	0.072	49.741
Manbulloo S1	784.65	-0.173	0.089	14.434
Manbulloo S1	789.46	-0.158	0.117	20.127
Manbulloo S1	865.8	-0.136	0.119	15.103
GRNT-79-4	153.4	-0.161	0.080	17.833
GRNT-79-7	657.6	-0.156	0.069	15.447
GRNT-79-7	668.4	-0.120	0.109	65.133
GRNT-79-7	678	-0.264	0.056	38.588
GRNT-79-7	792	-0.224	0.086	9.435
GRNT-79-7	812.6	-0.106	0.057	1.088
GRNT-79-7	891	-0.214	0.069	2.484

Table A10: δ^{53}Cr values for NIST SRM 979 analytical standards run alongside samples on the TIMS. True values are 0‰, but instrumental offset means an average δ^{53}Cr values needs to be subtracted from calculated values for samples. The table above shows values that have already been corrected for this.

Date Analysed	δ^{53}Cr (‰)	δ^{53}Cr error (‰)
3/09/2019	0.915	0.047
3/09/2019	0.884	0.051
5/09/2019	0.770	0.055
5/09/2019	0.849	0.043
10/09/2019	0.888	0.100
30/09/2019	0.779	0.073
20/09/2019	0.714	0.063
Average offset	0.8284	

Greater McArthur Basin major and trace element data

Table A11: Concentrations of elements with masses 24 to 53 in shales from the greater McArthur Basin. Blue, red, purple and yellow colouring indicates the Velkerri, Mainoru, Fraynes and Barney Creek Formations respectively.

Drill Hole ID	Depth (m)	^{24}Mg (ppm)	^{27}Al (ppm)	$^{31\rightarrow47}$P (ppm)	$^{43\rightarrow59}$Ca (ppm)	$^{44\rightarrow60}$Ca (ppm)	^{45}Sc (ppm)	^{47}Ti (ppm)	^{49}Ti (ppm)	^{51}V (ppm)	^{52}Cr (ppm)	^{53}Cr (ppm)
Altree 2	640.98	2215.89	2701.31	1164.79	6115.50	7465.24	1.59	33.27	33.22	6.59	2.95	2.72
Altree 2	664.69	19410.57	2117.93	1974.65	85879.59	103918.62	6.06	30.32	31.57	39.73	2.65	2.29
Altree 2	760.33	1312.69	2959.60	1784.73	7755.94	9361.32	1.73	30.80	32.66	18.05	3.01	2.68
Marmbulligan 1	214.3	1759.84	5890.06	811.43	34969.72	44534.71	2.84	88.44	90.12	22.58	14.52	12.83
Tanumbirini 1	3199	962.86	3206.00	2619.99	9347.04	10866.54	1.92	12.67	13.10	8.47	52.89	46.34
Urapunga 5	401.5	2157.91	7626.14	98.22	8166.26	9099.51	2.17	49.48	38.68	8.11	6.62	5.73
Urapunga 5	439.65	5108.84	11598.41	169.73	10934.05	11784.81	4.19	68.63	72.54	14.01	9.34	8.13
Urapunga 5	487.5	3229.32	6375.85	208.87	12820.73	14394.52	2.88	40.34	37.71	7.62	4.87	4.19
Urapunga 5	563.1	1550.53	7984.37	312.07	-	-	3.07	43.01	33.67	8.92	5.85	5.09
Urapunga 5	597.8	2049.82	9081.16	577.21	-	1959.23	3.57	125.74	103.30	12.28	8.20	7.15
Urapunga 6	251.4	2970.80	8141.10	244.64	113631.46	140821.79	3.72	36.62	34.41	16.70	7.30	6.25
Manbulloo S1	722.99	60860.03	723.44	182.75	197680.02	243833.86	2.98	6.10	6.79	6.37	2.50	2.20
Manbulloo S1	781.7	42462.54	1460.18	674.78	144807.72	182076.53	4.36	20.29	23.71	13.78	3.44	2.97
Manbulloo S1	783.54	2798.40	1401.53	1116.97	14680.85	16056.32	1.66	13.69	14.63	6.44	1.71	1.54
Manbulloo S1	784.65	8809.87	1774.17	1973.82	35508.60	45491.62	3.65	30.10	42.77	7.15	2.50	2.06
Manbulloo S1	789.46	15604.80	1578.92	1648.35	64146.72	80044.79	3.07	16.03	17.79	8.96	2.24	1.89
Manbulloo S1	865.8	566.02	1525.16	103.17	20312.26	21830.96	0.85	7.03	9.30	1.35	1.15	1.02
GRNT-79-4	153.4	11011.62	7533.49	722.02	33831.64	42702.97	3.36	41.36	40.98	26.46	9.23	8.02
GRNT-79-7	657.6	37897.48	5334.16	842.78	157343.37	192283.96	3.61	59.31	111.71	13.44	6.78	5.89
GRNT-79-7	668.4	30011.00	4594.51	584.47	112047.45	139429.07	3.24	56.31	49.57	12.63	4.57	4.06
GRNT-79-7	678	39341.58	4527.72	535.98	167345.69	204470.88	3.02	50.69	49.63	14.70	5.09	4.52
GRNT-79-7	792	28283.52	4906.76	974.13	97949.08	118829.83	3.82	49.76	50.85	14.98	5.44	4.81
GRNT-79-7	812.6	24246.60	5445.36	876.47	100918.01	123524.84	3.84	78.42	61.17	18.03	5.51	4.84
GRNT-79-7	891	5844.77	4679.51	1166.48	20585.84	22652.17	3.04	68.30	52.80	18.32	6.96	5.89

Table A12: Concentrations of elements with masses 55 to 89 in shales from the greater McArthur Basin. Blue, red, purple and yellow colouring indicates the Velkerri, Mainoru, Fraynes and Barney Creek Formations respectively.

Drill Hole ID	Depth (m)	^{55}Mn (ppm)	$^{56\rightarrow72}$Fe (ppm)	$^{57\rightarrow73}$Fe (ppm)	^{59}Co (ppm)	^{60}Ni (ppm)	^{63}Cu (ppm)	^{66}Zn (ppm)	^{71}Ga (ppm)	^{85}Rb (ppm)	^{88}Sr (ppm)	^{89}Y (ppm)
Altree 2	640.98	38.55	4339.28	4399.29	13.83	47.02	94.37	497.01	1.10	14.11	13.42	10.27
Altree 2	664.69	747.78	15554.71	16592.23	7.34	45.83	78.16	230.15	1.06	10.14	83.88	26.35
Altree 2	760.33	38.24	3526.98	3526.05	6.66	21.76	65.75	283.94	1.26	16.42	29.46	14.69
Marmbulligan 1	214.3	48.40	5280.74	5255.88	5.62	18.93	26.19	1811.74	2.16	26.14	44.27	7.92
Tanumbirini 1	3199	31.85	4541.31	4604.99	7.22	16.99	112.46	266.92	1.46	12.90	65.23	25.03
Urapunga 5	401.5	182.16	6977.34	7063.13	17.90	4.01	7.91	623.49	2.19	29.61	23.27	2.43
Urapunga 5	439.65	4405.96	9511.47	9585.34	53.60	5.82	11.76	27.19	3.50	38.76	18.18	6.94
Urapunga 5	487.5	13661.49	9687.06	9889.53	14.74	4.31	3.14	224.24	1.86	37.26	26.01	6.93
Urapunga 5	563.1	101.65	4395.34	4427.97	24.92	8.03	10.67	43.03	2.31	31.25	18.94	4.57
Urapunga 5	597.8	111.33	5952.68	6027.57	13.93	2.73	12.73	184.05	3.15	35.86	22.62	13.69
Urapunga 6	251.4	4785.84	94221.78	103518.62	32.77	6.04	3.62	3673.49	2.11	17.71	87.89	6.39
Manbulloo S1	722.99	522.66	4842.06	4831.44	16.82	3.75	1.34	673.49	0.53	3.94	50.61	11.87
Manbulloo S1	781.7	579.03	7252.61	7232.15	14.30	4.46	11.74	401.65	0.90	6.71	28.10	15.08
Manbulloo S1	783.54	46.11	1041.30	1023.53	11.94	6.64	11.84	662.31	0.76	8.52	15.50	6.62
Manbulloo S1	784.65	121.27	2538.10	2514.38	12.43	10.47	15.46	344.16	1.08	10.72	22.73	13.63
Manbulloo S1	789.46	257.19	2814.32	2799.75	9.18	10.66	6.31	371.45	1.02	7.96	28.71	15.60
Manbulloo S1	865.8	21.88	666.73	662.78	6.16	7.03	9.39	759.43	0.36	10.08	19.55	0.74
GRNT-79-4	153.4	500.10	3988.23	4026.78	16.65	12.07	21.85	928.27	2.96	20.83	32.15	10.16
GRNT-79-7	657.6	348.63	5381.14	5402.16	9.69	10.01	12.14	1085.76	2.19	26.33	79.40	16.42
GRNT-79-7	668.4	343.77	4952.22	4939.58	5.97	8.18	11.18	247.30	1.95	23.91	56.51	13.32
GRNT-79-7	678	388.18	5459.71	5422.30	5.69	7.16	10.38	142.29	1.96	20.36	88.65	14.21
GRNT-79-7	792	459.53	5496.84	5450.04	7.39	8.29	19.87	461.64	2.05	26.43	54.97	14.21
GRNT-79-7	812.6	521.75	5523.23	5517.31	6.90	9.23	5.99	842.48	2.27	27.29	59.41	17.00
GRNT-79-7	891	1087.10	4723.53	4701.08	20.62	18.12	22.86	214.02	1.98	25.11	32.99	15.53

Table A13: Concentrations of elements with masses 90 to 153 in shales from the greater McArthur Basin. Blue, red, purple and yellow colouring indicates the Velkerri, Mainoru, Fraynes and Barney Creek Formations respectively.

Drill Hole ID	Depth (m)	^{90}Zr (ppm)	^{95}Mo (ppm)	^{90}Mo (ppm)	^{133}Cs (ppm)	^{137}Ba (ppm)	^{139}La (ppm)	^{140}Ce (ppm)	^{141}Pr (ppm)	^{146}Nd (ppm)	^{147}Sm (ppm)	^{153}Eu (ppm)
Altree 2	640.98	0.59	1.21	1.27	0.75	3.80	1.90	6.62	1.38	8.41	3.72	0.71
Altree 2	664.69	1.67	7.45	7.42	0.43	43.01	7.79	19.47	3.69	17.75	5.48	1.06
Altree 2	760.33	1.15	12.62	12.60	1.21	95.50	3.72	9.76	1.92	11.43	5.42	1.12
Marmbulligan 1	214.3	1.26	7.28	7.42	1.19	84.32	3.12	8.94	1.63	8.66	3.26	0.69
Tanumbirini 1	3199	0.89	3.49	3.42	1.37	182.59	9.20	22.59	3.96	18.96	6.68	1.50
Urapunga 5	401.5	2.54	-	-	1.07	79.56	4.05	8.54	1.07	4.47	1.16	0.22
Urapunga 5	439.65	2.40	-	-	0.93	99.34	4.82	14.64	1.78	7.63	2.70	0.54
Urapunga 5	487.5	2.32	-	-	2.48	268.31	3.28	11.98	1.49	7.45	2.41	0.51
Urapunga 5	563.1	2.15	0.28	0.28	1.16	99.82	3.22	9.59	1.38	6.69	2.33	0.42
Urapunga 5	597.8	5.43	-	-	1.78	93.65	6.83	21.12	3.29	16.24	6.50	1.27
Urapunga 6	251.4	0.84	0.44	0.47	0.84	71.76	3.15	7.69	1.01	3.90	0.96	0.21
Manbulloo S1	722.99	0.89	1.24	1.30	0.21	11.23	9.81	21.86	2.50	9.46	1.94	0.33
Manbulloo S1	781.7	1.22	3.02	2.99	0.51	8.16	10.39	26.49	3.68	15.25	3.43	0.61
Manbulloo S1	783.54	1.04	7.79	7.88	0.82	6.27	7.01	19.51	2.89	12.25	2.56	0.37
Manbulloo S1	784.65	2.68	11.99	12.07	0.90	9.40	9.53	29.13	4.33	19.01	4.58	0.70
Manbulloo S1	789.46	2.02	7.95	8.05	0.75	7.89	9.81	28.37	4.24	18.04	4.07	0.62
Manbulloo S1	865.8	0.76	-	-	1.51	5.51	0.51	1.06	0.20	1.17	0.78	0.14
GRNT-79-4	153.4	3.03	0.96	0.95	0.29	105.75	14.20	35.86	4.73	18.75	3.80	0.56
GRNT-79-7	657.6	2.92	3.26	3.33	1.06	190.98	14.90	33.17	4.66	18.94	4.20	0.68
GRNT-79-7	668.4	2.34	2.39	2.47	0.89	61.75	12.79	28.63	3.74	15.21	3.25	0.53
GRNT-79-7	678	2.53	4.65	4.62	0.62	125.08	13.80	29.03	3.88	15.30	3.24	0.54
GRNT-79-7	792	1.88	1.12	1.10	0.86	23.24	11.13	28.22	4.01	16.95	3.99	0.65
GRNT-79-7	812.6	2.58	1.68	1.69	0.91	24.14	12.94	28.92	4.07	16.73	3.83	0.56
GRNT-79-7	891	2.91	0.64	0.66	1.77	133.04	11.11	36.61	4.39	18.71	4.57	0.75

Table A14: Concentrations of elements with masses 153 to 166 in shales from the greater McArthur Basin. Blue, red, purple and yellow colouring indicates the Velkerri, Mainoru, Fraynes and Barney Creek Formations respectively.

Drill Hole ID	Depth (m)	$^{153\rightarrow169}$Eu (ppm)	^{157}Gd (ppm)	$^{157\rightarrow173}$Gd (ppm)	^{159}Tb (ppm)	$^{159\rightarrow175}$Tb (ppm)	^{163}Dy (ppm)	$^{163\rightarrow179}$Dy (ppm)	^{165}Ho (ppm)	$^{165\rightarrow181}$Ho (ppm)	^{166}Er (ppm)	$^{166\rightarrow182}$Er (ppm)
Altree 2	640.98	0.61	4.28	4.35	0.53	0.53	2.26	2.33	0.35	0.36	0.77	0.76
Altree 2	664.69	0.89	5.71	5.73	0.84	0.83	4.60	4.59	0.85	0.85	2.08	2.06
Altree 2	760.33	0.97	6.06	6.17	0.70	0.72	3.17	3.19	0.49	0.50	1.04	1.05
Marmbulligan 1	214.3	0.59	3.46	3.50	0.42	0.40	1.78	1.73	0.27	0.27	0.54	0.54
Tanumbirini 1	3199	1.19	9.00	8.75	1.24	1.17	5.76	5.55	0.92	0.90	2.12	2.05
Urapunga 5	401.5	0.20	1.03	1.08	0.13	0.12	0.53	0.59	0.09	0.10	0.21	0.23
Urapunga 5	439.65	0.43	2.46	2.38	0.32	0.29	1.46	1.45	0.24	0.23	0.59	0.55
Urapunga 5	487.5	0.39	2.08	1.98	0.27	0.25	1.34	1.25	0.23	0.22	0.61	0.58
Urapunga 5	563.1	0.34	2.17	2.09	0.24	0.23	1.05	0.98	0.16	0.16	0.35	0.33
Urapunga 5	597.8	1.03	7.03	6.79	0.84	0.79	3.48	3.30	0.48	0.46	0.88	0.85
Urapunga 6	251.4	0.16	1.09	1.06	0.18	0.18	1.09	1.08	0.23	0.23	0.64	0.64
Manbulloo S1	722.99	0.22	1.89	1.77	0.31	0.29	1.92	1.75	0.37	0.36	1.04	0.98
Manbulloo S1	781.7	0.51	3.28	3.13	0.48	0.44	2.64	2.50	0.47	0.47	1.24	1.19
Manbulloo S1	783.54	0.32	2.17	2.11	0.27	0.26	1.32	1.27	0.21	0.22	0.48	0.47
Manbulloo S1	784.65	0.57	3.98	3.98	0.50	0.49	2.48	2.47	0.40	0.41	0.94	0.94
Manbulloo S1	789.46	0.53	3.63	3.55	0.49	0.47	2.59	2.57	0.48	0.48	1.27	1.26
Manbulloo S1	865.8	0.11	0.58	0.59	0.05	0.05	0.20	0.21	0.03	0.03	0.06	0.07
GRNT-79-4	153.4	0.44	3.31	3.18	0.43	0.40	2.08	2.01	0.35	0.34	0.83	0.78
GRNT-79-7	657.6	0.54	3.82	3.67	0.51	0.49	2.71	2.63	0.50	0.49	1.29	1.27
GRNT-79-7	668.4	0.45	3.01	2.95	0.41	0.39	2.21	2.17	0.41	0.41	1.07	1.05
GRNT-79-7	678	0.44	2.92	2.83	0.41	0.38	2.23	2.11	0.42	0.41	1.12	1.09
GRNT-79-7	792	0.52	3.67	3.61	0.50	0.46	2.51	2.46	0.45	0.43	1.10	1.05
GRNT-79-7	812.6	0.46	3.64	3.51	0.50	0.49	2.75	2.68	0.51	0.51	1.37	1.35
GRNT-79-7	891	0.61	4.41	4.22	0.59	0.55	2.96	2.85	0.49	0.49	1.17	1.14

Table A15: Concentrations of elements with masses 169 to 238 in shales from the greater McArthur Basin. Blue, red, purple and yellow colouring indicates the Velkerri, Mainoru, Fraynes and Barney Creek Formations respectively.

Drill Hole ID	Depth (m)	^{169}Tm (ppm)	$^{169\rightarrow185}$Tm (ppm)	^{172}Yb (ppm)	$^{172\rightarrow188}$Yb (ppm)	^{175}Lu (ppm)	$^{175\rightarrow191}$Lu (ppm)	^{178}Hf (ppm)	^{208}Pb (ppm)	^{232}Th (ppm)	^{238}U (ppm)
Altree 2	640.98	0.08	0.08	0.43	0.37	0.06	0.06	0.03	2.70	3.41	0.55
Altree 2	664.69	0.24	0.24	1.40	1.21	0.20	0.19	0.10	27.35	3.75	0.63
Altree 2	760.33	0.11	0.11	0.58	0.48	0.07	0.07	0.07	3.00	4.45	1.95
Marmbulligan 1	214.3	0.06	0.05	0.30	0.24	0.04	0.04	0.04	12.00	4.82	0.91
Tanumbirini 1	3199	0.25	0.24	1.48	1.21	0.21	0.19	0.02	28.61	5.93	0.91
Urapunga 5	401.5	0.04	0.03	0.16	0.16	0.02	0.02	0.11	2.54	3.30	0.41
Urapunga 5	439.65	0.07	0.07	0.43	0.37	0.05	0.05	0.12	23.62	3.88	0.39
Urapunga 5	487.5	0.08	0.08	0.53	0.46	0.07	0.06	0.13	1.26	2.50	0.11
Urapunga 5	563.1	0.04	0.04	0.23	0.17	0.03	0.03	0.10	14.58	3.69	0.33
Urapunga 5	597.8	0.09	0.08	0.38	0.33	0.05	0.04	0.14	2.35	7.86	0.46
Urapunga 6	251.4	0.09	0.09	0.59	0.48	0.08	0.08	0.04	33.87	1.45	0.80
Manbulloo S1	722.99	0.13	0.12	0.83	0.76	0.12	0.11	0.05	6.49	1.56	1.02
Manbulloo S1	781.7	0.17	0.15	0.95	0.80	0.13	0.13	0.06	11.10	1.94	0.29
Manbulloo S1	783.54	0.05	0.05	0.28	0.26	0.04	0.04	0.04	11.36	1.81	0.30
Manbulloo S1	784.65	0.10	0.10	0.52	0.44	0.07	0.07	0.14	15.07	2.79	0.86
Manbulloo S1	789.46	0.16	0.16	0.96	0.90	0.14	0.14	0.07	12.40	3.01	0.39
Manbulloo S1	865.8	0.01	-	0.04	0.05	0.01	0.01	0.03	8.72	0.45	0.09
GRNT-79-4	153.4	0.10	0.09	0.58	0.51	0.08	0.08	0.12	6.37	4.02	0.43
GRNT-79-7	657.6	0.16	0.17	1.05	0.90	0.15	0.14	0.15	13.94	3.44	0.83
GRNT-79-7	668.4	0.14	0.14	0.86	0.72	0.12	0.12	0.13	14.58	2.85	0.61
GRNT-79-7	678	0.15	0.15	0.91	0.85	0.14	0.13	0.13	13.73	2.85	0.75
GRNT-79-7	792	0.13	0.13	0.78	0.66	0.11	0.11	0.10	10.56	2.99	0.52
GRNT-79-7	812.6	0.18	0.18	1.11	0.89	0.16	0.15	0.12	16.10	3.02	0.46
GRNT-79-7	891	0.14	0.14	0.87	0.76	0.13	0.12	0.12	37.95	3.58	0.32

APPENDIX E: RAYLEIGH MODELS

Coorong nitrogen isotopes

Using the Rayleigh fractionation equation

$$\delta^{15}N_{reactant} = \delta^{15}N_{initial} + \varepsilon(1 - f)$$

Where $\delta^{15}N$ refers to the isotopic composition of NH_4^+, ε is the kinetic isotope effect of the transformation and defined as $\delta^{15}N_{product} - \delta^{15}N_{reactant}$ and f is the fraction of reactant remaining (Sigman, Karsh, & Casciotti, 2009).

Table A16: Calculations for the Rayleigh fractionation of NH_4^+ in the Coorong, using 3 different models for fractionation. The first models biological consumption (De Brabandere, Brion, Elskens, Baeyens, & Dehairs, 2007), the second uses the upper limit to average fractionations observed for DNRA (Casciotti, 2016), and the third uses the maximum value for volatilisation (Stüeken, Kipp, Koehler, & Buick, 2016). The initial value is taken to be the isotopic composition measured at Salt Creek.

		Biological consumption		DNRA		Volatilisation	
f (%)	$\delta^{15}N_{initial}$ (‰)	ε (‰)	$\delta^{15}N_{reactant}$ (‰)	ε (‰)	$\delta^{15}N_{reactant}$ (‰)	ε (‰)	$\delta^{15}N_{reactant}$ (‰)
1	6.3	18.4	6.3	30	6.3	45	6.3
0.9	6.3	18.4	8.1	30	9.3	45	11.0
0.8	6.3	18.4	10.0	30	12.3	45	16.3
0.7	6.3	18.4	11.8	30	15.3	45	22.4
0.6	6.3	18.4	13.7	30	18.3	45	29.3
0.5	6.3	18.4	15.5	30	21.3	45	37.5
0.4	6.3	18.4	17.3	30	24.3	45	47.5
0.3	6.3	18.4	19.2	30	27.3	45	60.5
0.2	6.3	18.4	21.0	30	30.3	45	78.7
0.1	6.3	18.4	22.9	30	33.3	45	109.9
0.05	6.3	18.4	23.8	30	34.8	45	141.1
0.025	6.3	18.4	24.2	30	35.6	45	172.3
0.01	6.3	18.4	24.5	30	36.0	45	213.5
0.005	6.3	18.4	24.6	30	36.2	45	244.7

McArthur Basin chromium isotopes

Using the Rayleigh fractionation equation

$$\delta^{53}\mathrm{Cr}_{\mathrm{unreacted}} = [(\delta^{53}\mathrm{Cr}_{\mathrm{initial}} + 10^3)\, f^{(\alpha-1)}] - 10^3$$

Where f is the fraction of reactant remaining and α is the instantaneous fractionation factor. The α value is defined as $R_{prod} - R_{react}$, where R_{prod} and R_{react} are the $^{53}Cr/^{52}Cr$ ratios of the instantaneously reduced Cr and that in the reactant pool, respectively (Ellis, Johnson, & Bullen, 2002). Alternately, α can be defined as α = (ε /1000) + 1 where ε is the kinetic isotope effect (Bauer et al., 2018).

Table A17: Calculations for the Rayleigh fractionation of Cr in the greater McArthur Basin, using 3 different models for fractionation. The first uses ε = -0.8‰, the value typically accepted for modern oceans worldwide (Scheiderich, Amini, Holmden, & Francois, 2015). The second models reduction by organic reductants, using ε = -3.11‰ (Kitchen, Johnson, Bullen, Zhu, & Raddatz, 2012). The third comparatively uses α = 0.9985, interpreted to be from the combined effect of homogenous reduction by $Cr(VI)_{aq}$ followed by the reduction of intercalated Cr(VI) by Fe(II) (Døssing, Dideriksen, Stipp, & Frei, 2011). These models all assume a $\delta^{53}Cr_{initial}$ value of 0‰ for simplicity, although continental run-off and surface water can have different isotopic values (Bauer et al., 2018).

		Average modern ocean		Organic reductants		Combined Cr and Fe(II) reduction	
***f* (%)**	**$\delta^{53}Cr_{unreacted}$ (‰)**	**ε (‰)**	**$\delta^{53}Cr_{unreacted}$ (‰)**	**ε (‰)**	**$\delta^{53}Cr_{unreacted}$ (‰)**	**α**	**$\delta^{53}Cr_{unreacted}$ (‰)**
1	0	0.9992	0.0	0.99689	0.0	0.9985	0.0
0.9	0	0.9992	0.1	0.99689	0.3	0.9985	0.2
0.8	0	0.9992	0.2	0.99689	0.7	0.9985	0.3
0.7	0	0.9992	0.3	0.99689	1.1	0.9985	0.5
0.6	0	0.9992	0.4	0.99689	1.6	0.9985	0.8
0.5	0	0.9992	0.6	0.99689	2.2	0.9985	1.0
0.4	0	0.9992	0.7	0.99689	2.9	0.9985	1.4
0.3	0	0.9992	1.0	0.99689	3.8	0.9985	1.8
0.2	0	0.9992	1.3	0.99689	5.0	0.9985	2.4
0.1	0	0.9992	1.8	0.99689	7.2	0.9985	3.5
0.05	0	0.9992	2.4	0.99689	9.4	0.9985	4.5
0.025	0	0.9992	3.0	0.99689	11.5	0.9985	5.5
0.01	0	0.9992	3.7	0.99689	14.4	0.9985	6.9
0.005	0	0.9992	4.2	0.99689	16.6	0.9985	8.0

APPENDIX REFERENCES

AMERICAN PUBLIC HEALTH ASSOCIATION, AMERICAN WATER WORKS ASSOCIATION, & WATER ENVIRONMENT FEDERATION. (2005). *Standard methods for the examination of water and wastewater* (21st ed.). Washington D.C.: APHA-AWWA-WEF.

BAUER, K. W., GUEGUEN, B., COLE, D. B., FRANCOIS, R., KALLMEYER, J., PLANAVSKY, N., & CROWE, S. A. (2018). Chromium isotope fractionation in ferruginous sediments. *Geochimica et Cosmochimica Acta, 223*, 198-215. doi:10.1016/j.gca.2017.10.034

BIRTE FRANK, A. (2019). *Chromium isotopes variations in black shales: Evaluating the applicability of chromium stable isotope signatures of ancient black shales as a paleoredox archive.* (Doctor of Philosophy Ph.D. Thesis), University of Copenhagen, Denmark.

BRUGGMAN, S. (2018). *Assessing the potential of the chromium isotope system to record redox changes.* (Doctor of Philosophy Ph.D. Thesis), University of Copenhagen, Denmark.

CASCIOTTI, K. L. (2016). Nitrogen and oxygen isotopic studies of the marine nitrogen cycle. *Annual Review of Marine Science, 8*(1), 379-407. doi:10.1146/annurev-marine-010213-135052

DE BRABANDERE, L., BRION, N., ELSKENS, M., BAEYENS, W., & DEHAIRS, F. (2007). $\delta^{15}N$ dynamics of ammonium and particulate nitrogen in a temperate eutrophic estuary. *Biogeochemistry, 82*(1), 1-14. doi:10.1007/s10533-006-9047-1

DØSSING, L. N., DIDERIKSEN, K., STIPP, S. L. S., & FREI, R. (2011). Reduction of hexavalent chromium by ferrous iron: A process of chromium isotope fractionation and its relevance to natural environments. *Chemical Geology, 285*(1), 157-166. doi:10.1016/j.chemgeo.2011.04.005

ELLIS, A. S., JOHNSON, T. M., & BULLEN, T. D. (2002). Chromium isotopes and the fate of hexavalent chromium in the environment. *Science (New York, N.Y.), 295*(5562), 2060. doi:10.1126/science.1068368

KITCHEN, J. W., JOHNSON, T. M., BULLEN, T. D., ZHU, J., & RADDATZ, A. (2012). Chromium isotope fractionation factors for reduction of Cr(VI) by aqueous Fe(II) and organic molecules. *Geochimica et Cosmochimica Acta, 89*, 190-201. doi:10.1016/j.gca.2012.04.049

RUSSELL, D. G., WONG, W. W., & COOK, P. L. M. (2018). Negligible isotopic fractionation of nitrogen within temperate *Zostera* spp. meadows. *Biogeosciences Discussions, 15*(23), 7225-7234. doi:10.5194/bg-2018-154

SCHEIDERICH, K., AMINI, M., HOLMDEN, C., & FRANCOIS, R. (2015). Global variability of chromium isotopes in seawater demonstrated by Pacific, Atlantic, and Arctic Ocean samples. *Earth and Planetary Science Letters, 423*, 87-97. doi:10.1016/j.epsl.2015.04.030

SIGMAN, D., KARSH, K., & CASCIOTTI, K. L. (2009). Ocean process tracers: Nitrogen isotopes in the ocean. In J. H. Steele, Turekian, K. K., and Thorpe, S. A. (Ed.), *Encyclopedia of Ocean Sciences*: Academic Press.

STÜEKEN, E. E., KIPP, M. A., KOEHLER, M. C., & BUICK, R. (2016). The evolution of Earth's biogeochemical nitrogen cycle. *Earth-Science Reviews, 160*(C), 220-239. doi:10.1016/j.earscirev.2016.07.007

TOLEDO, G. E. (2018). *Chromium isotope constraints on the Mid-Proterozoic redox: Evidence from $\delta^{53}Cr$ of carbonates from the Greater McArthur Basin, Northern Australia.* (Honours Degree in Geology), The University of Adelaide, Adelaide.

WONG, W. W., POTTAGE, J., WARRY, F. Y., REICH, P., ROBERTS, K. L., GRACE, M. R., & COOK, P. L. M. (2018). Stable isotopes of nitrate reveal different nitrogen processing mechanisms in streams across a land use gradient during wet and dry periods. *Biogeosciences, 15*(13), 3953-3965. doi:10.5194/bg-15-3953-2018

ZHANG, L., ALTABET, M. A., WU, T., & HADAS, O. (2007). Sensitive measurement of NH_4^+ $^{15}N/^{14}N$ ($\delta^{15}NH_4^+$) at natural abundance levels in fresh and saltwaters. *Analytical Chemistry, 79*(14), 5297-5303. doi:10.1021/ac070106d